Journal of Atmospheric and Solar–Terrestrial Physics 246 (2023) 106055

Contents lists available at ScienceDirect

Journal of Atmospheric and Solar–Terrestrial Physics

journal homepage: www.elsevier.com/locate/jastp

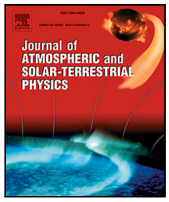

Research paper

Night light polarization: Modeling and observations of light pollution in the presence of aerosols and background skylight or airglow

Léo Bosse [a,b,*], Jean Lilensten [a,f], Nicolas Gillet [c], Colette Brogniez [d], Olivier Pujol [d], Sylvain Rochat [a], Alain Delboulbé [a], Stéphane Curaba [a], Magnar G. Johnsen [e]

[a] Univ. Grenoble Alpes, CNRS, IPAG, 38000 Grenoble, France
[b] BIRA-IASB, 3 Avenue Circulaire, Brussels, 1180, Belgium
[c] Univ. Grenoble Alpes, Univ. Savoie Mont Blanc, CNRS, IRD, Univ. Gustave Eiffel, ISTerre, Grenoble, 38000, France
[d] Univ. Lille, CNRS, UMR 8518, LOA - Laboratoire d'Optique Atmosphérique, F-59000 Lille, France
[e] Tromsø Geophysical Observatory, UiT - the Arctic University of Norway, Tromsø, N-9037, Norway
[f] Honorary astronomer at Royal Observatory of Belgium, 3 Avenue Circulaire, Brussels, 1180, Belgium

ARTICLE INFO

Dataset link: https://github.com/LeoBosse/analysis/tree/master/pomerol, https://eogdata.mines.edu/products/vnl/, http://eodg.atm.ox.ac.uk/RFM/atm/, https://www.eorc.jaxa.jp/ALOS/en/index_e.htm

MSC:
85A25
86A10

Keywords:
Polarized radiative transfer
Night lights
Pollution
Mesospheric emissions

ABSTRACT

We introduce a new polarized radiative transfer model able to compute the polarization measured by a virtual instrument in a given nocturnal environment recreating real world conditions (1-dimensional atmospheric and aerosol profiles, 3-dimensional light sources with complex and widespread geometries, terrain obstructions). Initially developed to address the issue of aurorae and nightglow polarization, the model has potential applications in the context of light pollution, or aerosols and air pollution measurements in night time conditions. We provide the physical assumptions behind the model together with the main points regarding its numerical implementation, together with the inherent constraints and liberties it brings. The model, based on single scattering equations in the atmosphere, is first tested on a few simple configurations to assess the effect of several key parameters in controlled environments. The model outputs are then compared to field measurements obtained in four wavelengths at mid-latitude in a dark valley of the French Alps, 20 km away from the closest city. In this context where the nightglow emissions are supposedly stationary and widespread, a convincing fit between the model predictions and observations is found in three wavelengths. This confrontation of ground-based records with our modeling constitutes a proof of concept for the investigation of our polarized environment in nocturnal conditions, in the presence of localized and/or extended sources. It calls for further investigations. In particular we discuss the future need for inter-calibrating the sources and the polarimeter in order to optimally extract the information contained in such measurements, and how multiple-scattering (not implemented in the present study) could impact our observations and their interpretation.

1. Introduction

The main auroral emissions are due to the atomic oxygen and molecular ion nitrogen N_2^+. The former produces the red (630 nm) and green (557.7 nm) light at the altitudes of about 220 and 110 km respectively. The latter emits in a large band amongst which the most prominent emissions are the blue (427.8 nm) and the purple (391.4 nm) radiation, around an altitude of 85 km. They mainly originate in the collisions between precipitated electrons and the ambient atmosphere (see for example Banks and Kockarts, 1973).

These emissions are pronounced at high latitudes, in the auroral ovals. They also exist at lower latitudes, where they are called *nightglow* (Leinert et al., 1998). The literature is abundant and here we only refer to some recent works. Emissions exist at all latitudes (Parihar et al., 2018). Their origin is due to chemical reactions (Plane et al., 2012) and collisions, either between neutral molecules or atoms, or between ambient ionospheric electrons and gases (Tashchilin and Leonovich, 2016). Even though some of these are always present, brighter emissions can be linked to the presence of gravity waves (Vargas, 2019) or ionospheric currents (Dymond et al., 2019).

For the last decade, a series of experiments have shown that the red emission is polarized when measured from the ground (Lilensten et al., 2016, and references herein). The direction of polarization for this red line was shown theoretically to be parallel to the magnetic field (Bommier et al., 2011). Correlations between variations in the

* Corresponding author at: .
E-mail address: leo.bosse@aeronomie.be (L. Bosse).

https://doi.org/10.1016/j.jastp.2023.106055
Received 4 November 2022; Received in revised form 16 March 2023; Accepted 18 March 2023
Available online 28 March 2023
1364-6826/© 2023 Elsevier Ltd. All rights reserved.

magnetic field and in the angle of linear polarization ($AoLP$) had indeed been observed experimentally, but not systematically, with a first prototype of auroral polarimeter (Lilensten et al., 2008).

Recently, a new nightglow polarimeter has been developed in order to observe faint emissions (i.e. not limited to bright aurorae). It also allows to target simultaneously several atmospheric emissions (for a full description, see Bosse et al., 2020). Recent findings (Bosse et al., 2020, 2022a,b) lead us to reconsider our first understanding of the upper atmosphere polarization:

- All of the four auroral emission lines appear polarized when measured from the ground.
- Although in several circumstances this polarization appears to be linked to the local magnetic activity and to the state of the ionosphere, it is far from being systematically aligned to the apparent direction of the magnetic field, as foreseen theoretically. Instead an influence of electrical currents in the high atmosphere is suspected.
- Despite a necessary polarization near the emission sources, as shown experimentally (Bourgeois et al., 2022), light pollution from nearby cities significantly impacts, via scattering, the polarization measurements.

These series of observations questioned the geophysical origin of the polarization: how much is it affected by light pollution scattering in the lower atmosphere? Which part of auroral lights is polarized at the emission, and during their propagation towards the instrument? To answer these questions, it appeared necessary to develop a polarized radiative transfer code able to account for sources potentially spread all over both the sky and the ground.

In the present study, we describe the first code developed to this purpose, called 'POMEROL' (standing for 'POlarisation par Mie Et Rayleigh des Objets Lumineux', which translates to 'Luminous Objects Polarization by Mie and Rayleigh Scattering'). This code has been used by Bosse et al. (2022a) in another context. In this last study, the authors did not present the inner working and validation procedure of the model, but only the addition of complex auroral sources in the sky. One of the main characteristics of POMEROL is that it is able to take into account extended sources of faint lights either at ground (pollution light) or emitted in the sky (nightglow). It is also able to account for the ground topography. These conditions are very different from the usual studies of transfer of light in the atmosphere. Developing a dedicated numerical tool thus appeared to be more straightforward than considering already existing ones (Emde et al., 2015; Falchi et al., 2016; Berk and Hawes, 2017; Dudhia, 2017; Wang et al., 2020). Our model is then applied to ground-based polarimetric data obtained in the French Alps, in a configuration where the background sky emissions are simpler, more isotropic and constant, than in auroral conditions (Bosse et al., 2022a,b).

The code has been developed for assessing the impact of light pollution and radiative transfer onto high altitudes emissions. Its goal is to reproduce as much as possible the key features of ground-based observations (in particular the spatial distribution of wide-spread sources), while keeping the model set-up as simple as possible. The choices made for this initial version of the POMEROL have their associated limitations. In particular, it is restricted to the single scattering approximation (SSA). In this first attempt at modeling nocturnal ground-based polarization data, it appeared useful to assess how close POMEROL can fit observations within the SSA, before adding an extra layer of complexity by considering multiple scattering (MS). We show that even under the SSA, it is possible to explain a significant part of the measurements and to deduce physical parameters behind the polarization. However, we also discuss the limitations of this first approach, and what improvements could be brought by considering a polarized MS radiative transfer model.

Meanwhile, POMEROL in its initial version may already be used to address various issues. It indeed has potential applications outside the community studying the upper atmosphere. For instance it could help characterize aerosols in a passive experimental way in the absence of the Moon or the Sun. It may also improve the monitoring of light pollution, which represents a growing concern over the last decades. The area covered by light from human origin is spreading, along with its impacts on life (Grubisic et al., 2018), energy consumption (Kyba et al., 2017) or astronomy. Among the literature displaying a varied list of negative effects, we can cite the insect population decline and the "Ecological Armageddon" (Grubisic et al., 2018) or health issues (Garcia-Saenz et al., 2018; Zielinska-Dabkowska, 2018). Most of the studies concentrate on the brightness and spread of light pollution and we lack studies on its polarization (Kriska et al., 1998; Horvath et al., 2009; Kyba et al., 2011). Yet it plays an important role for vast groups of insects that use it to navigate.

As we will discuss later, POMEROL cannot be used out of the box for these applications today, as they may require specific features that our model lacks (such as a calibrated value for the sky radiance, or an implementation of MS). Such developments will be the focus of future works, if deemed necessary. In the meantime, we hope that the open-source version of POMEROL will help understand the night light polarization and the nocturnal environment.

The manuscript is organized as follows. We first briefly describe the instrument in Section 2. We then present the principles of the radiative transfer model in Section 3 (the full details are given in Appendix A). Next we provide in Section 4 a series of synthetic experiments in order to assess the influence of the input parameters: effect of a localized source on the ground and of atmospheric properties (ozone, aerosols). In Section 5, we compare the measurements from an experimental campaign at mid-latitude to the model outputs. Finally, we discuss our findings in Section 6, together with the strengths and limitations of our model.

2. Description of the polarimeter

Here is a brief overview of the experimental set-up. The polarimeter used in this study has been fully described in Bosse et al. (2020). We therefore only recall here its basics.

The incoming light along the line of sight is filtered through a narrow optical filter of 10 nm width. Behind it a polarizing lens rotates at 2 Hz. The light passing the lens then hits a photomultiplier and is converted into an electrical current with a 1 kHz sampling rate. Note that the detector is not calibrated and gives radiant flux values in arbitrary units. Therefore, the comparisons between models and data described in this article are all given in arbitrary units. Data are smoothed over a given time window during which the polarization is assumed constant (10 s for all data presented here). A lock-in analysis is performed in real time. This powerful method allows a fast and accurate computation of the polarization. However, when the degree of linear polarization ($DoLP$) becomes too small, typically below 0.5%, the $AoLP$ can hardly be computed and becomes very noisy. Both the $DoLP$ and $AoLP$ have been calibrated, but not the radiant flux.

We note F_0 the incident radiant flux received at a given wavelength (note that all units given in this paper follow the National Institute of Standards and Technology (NIST)). The $DoLP$ ranges between 0 and 1 (or, in the figures, 0 to 100%), and we define the $AoLP$ with respect to the vertical (0° being upward, ±90° horizontal as it is π-periodic). φ_t is the angle of the polarizing filter with the vertical at time t. We suppose that F_0, $DoLP$ and $AoLP$ do not change during one rotation of the polarizing filter. From basic optics, the radiant flux passing through the polarizing filter can be decomposed in two parts: a polarized one that varies as $\cos^2(\varphi_t - AoLP)$, and an unpolarized part, assumed to be constant over one rotation. For an incident radiant flux F_0, the polarized and unpolarized fluxes are

$$\begin{cases} F_0^{pola} = & DoLP \times F_0 \\ F_0^{unpola} = & (1 - DoLP) \times F_0 \,. \end{cases} \quad (1)$$

Following Malus Law, after the polarizing filter they become

$$\begin{cases} F_t^{pola} = & F_0^{pola}\cos^2(\varphi_t - AoLP) \\ F_t^{unpola} = & F_0^{unpola}/2\,. \end{cases} \quad (2)$$

The 1/2 factor on the unpolarized radiant flux comes from the averaging of Malus law over all $AoLP$. The radiant flux measured at time t can therefore be written as:

$$F_t = F_t^{pola} + F_t^{unpola} = F_0\left(DoLP \times \cos^2(\varphi_t - AoLP) + \frac{1 - DoLP}{2}\right). \quad (3)$$

Over one rotation of period T_r, this allows computing the Stokes parameters in spherical coordinates as:

$$\begin{cases} I &= \frac{1}{T_r}\int_0^{T_r} F_t dt \\ Q &= \frac{1}{T_r}\int_0^{T_r} F_t \cos 2\varphi_t dt \\ U &= -\frac{1}{T_r}\int_0^{T_r} F_t \sin 2\varphi_t dt\,. \end{cases} \quad (4)$$

Note that we do not consider circularly polarized light, such that the last Stokes parameter $V = 0$. This is for two reasons: the instruments we use do not measure circular polarization so that we cannot validate our model ; furthermore circular polarization is assumed to be small for Rayleigh and Mie scattering or at the emission in the upper atmosphere. It could easily be added to the model in the future if needed. The unit of the Stokes parameters as given here are nW, as it is the unit of the radiant flux measured by the instrument. To convert to nW/m^2/sr, we can simply divide them by the following coefficient depending on the instrument captor surface area Σ and half-opening angle ϵ: $2\pi\Sigma(1 - \cos(\epsilon))$. Injecting (3) in (4), one deduces the polarization parameters:

$$\begin{cases} F_0 &= 2I \\ DoLP &= \frac{2}{I}\sqrt{Q^2 + U^2} \\ AoLP &= \frac{1}{2}\arctan\left(\frac{U}{Q}\right). \end{cases} \quad (5)$$

The data may be smoothed over time by averaging I, Q and U over the desired number of rotations and then calculating the corresponding polarization values.

3. The radiative transfer model

In order to interpret the data from the instrument described in Section 2, we need to solve the polarized radiative transfer equations. This is the main goal of the POMEROL code which consists of two main sections: first modeling the radiative transfer equations, then applying the results to fit the data. We describe its inputs in Section 3.1 while the polarized radiative transfer equations are summarized in Section 3.2 and fully described in Appendix A. For the purpose of the present study, our analysis is based on single scattering. We aim at modeling the polarization observations under different configurations fitting the instrument observations. We thus consider several sources of light in four visible wavelengths: direct light (from the nightglow, or the starlight), and single scattered light (e.g. from cities, or auroral lights at high latitude).

3.1. Inputs of the model

3.1.1. Instrument related entries

The experimental characteristics are the first inputs, in particular the surface $\Sigma = 20$ cm^2 of the detector and its half aperture angle $\epsilon = 1°$, as well as its geographical position (latitude, longitude and altitude) and its pointing direction. This latter is defined by the elevation e (angle between the horizontal and the line of sight) and the azimuth a, reckoned with respect to the North, positive Eastward, i.e. clockwise rotation. One can specify discrete azimuths and elevations, or span over an *almucantar* (i.e. a full rotations in azimuth at a constant elevation) automatically. Latter on, we can also specify the radiant flux and polarization state observed by the instrument in a given direction, so that the model can adapt its parameters (e.g. aerosol model, background flux) to fit the data. The radiant flux measure of the instrument is not calibrated, and given in arbitrary units. This has consequences on the model implementation of the sources and the background light, as discussed later.

3.1.2. Cities and pollution map

The model also takes as input a light pollution map. These are 2-dimensional ground images of Earth at night produced by the NOAA Earth Observations Group, using satellite data from the Visible Infrared Imaging Radiometer Suite Day/Night Band. These images sum the emissions for wavelengths from 500 to 900 nm (Elvidge et al., 2013; Mills et al., 2013; Miller et al., 2013). The ground emissions are in units of nW/m^2/sr. The maps are processed to remove ephemeral light and are averaged over one year. They are provided by their authors in two modes, with the minimum emission set to zero or not. At high latitudes, auroral light are not always removed with other ephemeral lights, thus emission maps are overestimated. To better suppress the auroral contribution to the ground emission map, we use the second mode. At mid-latitude, the difference is minimal and we use the same mode for consistency. We use the most recent release from 2016. As the emission spectra of light pollution varies with location and time, we are unable to retrieve the radiance at each wavelength of interest. Thus, in the following, radiance unit is given in nW/m^2/sr and a linear intercalibration of the model output and the observational data in arbitrary units is needed. This method assumes that the spectra of all the lamps on the map are the same and that nearby cities all use the same kinds of lamps in the same proportions.

We also assume that the city lights are not polarized. Indeed, each pixel of the map spans thousands of square meters at minima, mixing a lot of sources, and there is no reason they all have a similar polarization.

The map is centered on the instrument in polar coordinates as depicted in Fig. 1. The maximum distance from the instrument (typically up to 200 km) and the number of bins (the best resolution being that of the map, namely 46 m) are adjustable parameters. To reduce artifacts due to digitization, the size of the bins increases with the square root of the distance to the instrument.

We can also consider instead synthetic emission maps. For example, these may consist of a point source of given radiance at a given distance, azimuth and elevation with respect to the instrument, or a uniform emission map of given radiance.

3.1.3. Natural background

In the following, the *natural background* light designates any source of light from the sky that we approximate as constant and isotropic. It includes two main contributions: the nightglow (Leinert et al., 1998) and the integrated starlight (e.g., Staude, 1975). The nightglow is specific as it is well defined in wavelengths (see Table 3). Its emissions can change with time and it can be highly structured. All-sky camera images, which are unfortunately not available for the present study, could be used to model the nightglow more accurately. The integrated starlight covers a wide spectrum over all observed wavelengths and is unpolarized. It varies with the time and place and could be recovered with astronomical tools in up-coming studies.

For now on, since the absolute values of these contributions are unknown, and also because the absolute radiant flux measured by the instrument is not calibrated, we cannot disentangle the several background contributions from the confrontation of our measurements with the model outputs. Thus, the background contribution may be considered to account for the model uncertainties. These are different for each wavelengths, time and location of observation. It is thus left

Table 1
Parameters used to define the aerosol model (see text for details).

Aerosol profile name	Complex refractive index		Size distribution		Vertical number density profile		
	Real	Imaginary	R (μm)	$ln(\sigma)$	H (m)	n_0 (cm^{-3})	n_B (cm^{-3})
1-low	1.45	0.0035	0.15	0.29	440	4000	10
2-high	1.61	0.03	0.557	0.266	500	1000	1
3-mid						500	

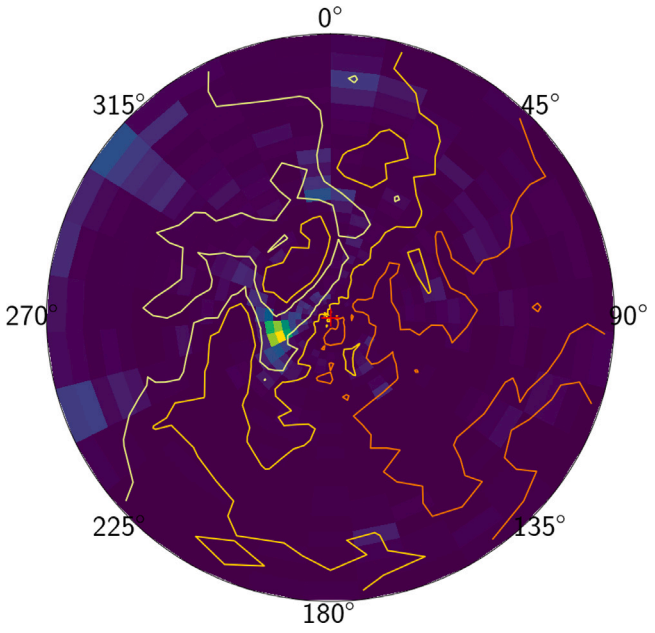

Fig. 1. Input emission map and contour of the elevation map for altitudes 500 m (white), 1000 m (yellow) and 2000 m (orange). The instrument is at the center of the map (red cross). Grenoble is the bright emission west to the instrument. The map covers 100 km around the instrument.

as a free parameter of the model for now on. It could be constrained by measurements or models in the future, if needed.

We note that no moonlight is considered in this study, as all measurements were done around the new Moon, when both the Moon and the Sun were at least 18 degrees below the horizon normally referred to as "astronomical twilight".

3.1.4. Atmospheric properties

To compute the Rayleigh scattering in the atmosphere, we need different atmospheric parameters. We use the 2001 MIPAS Model Atmospheres (Remedios et al., 2007) up to the lower thermosphere, at 120 km of altitude. It is a one dimensional model which provides the temperature $T(z)$ and pressure $P(z)$ vertical profiles (z is the altitude) as well as an ozone vertical profile. For the present purpose, we use their standard night-time mid-latitude profiles, displayed in Fig. 2.

To account for the influence of the aerosols, we consider a Lorenz–Mie scattering model (Lorenz, 1890; Mie, 1908; Born and Wolf, 1999; van de Hulst, 1981). This implies a wide range of input parameters, such as the complex refractive index, the aerosol sizes and their vertical profiles. Three aerosol models are considered in the present study, named 1-low, 2-high and 3-mid, whose parameters are listed in Table 1 (aerosol model names reflect the atmospheric aerosol content). We use complex optical indices from Dubovik et al. (2000) assumed to be the same for all wavelengths considered in this paper. The size distribution $n(\ln(r))$ of the aerosol is supposed to be log-normal,

$$n(ln(r)) = \frac{dN}{d\ln(r)} = \frac{N}{\sqrt{2\pi}\ln(\sigma)} \exp\left(-\frac{\ln^2(r/R)}{2\ln^2(\sigma)}\right), \quad (6)$$

Table 2
Optical depths of the atmospheric components for all wavelengths of interest. τ_{ray} is the optical depth of Rayleigh scattering, τ_{O3} is the optical depth of ozone and τ_{aer} is the optical depth of aerosols for the three aerosol models used in this study.

Wavelength (nm)	τ_{ray}	τ_{O_3}	τ_{aer} 1-low	τ_{aer} 2-high	τ_{aer} 3-mid
620.0	0.060	0.034	0.060	0.480	0.257
557.7	0.092	0.031	0.074	0.470	0.252
427.8	0.274	0.001	0.115	0.464	0.248
391.4	0.396	0.0002	0.129	0.461	0.247

with r the aerosol radius (in μm), N the total number of aerosols, R the mode radius (the radius where the distribution is maximal) and $\ln(\sigma)$ controlling the dispersion of the aerosol sizes around R. Below 12 km altitude, the vertical number density distribution of aerosol $n(z)$ is given by

$$n(z) = n_0 \left[\exp\left(\frac{-z}{H}\right) + \left(\frac{n_B}{n_0}\right)\right], \quad (7)$$

with n_0 the number density at the surface (in cm^{-3}), n_B the background number density (in cm^{-3}) and H the scale height (in m). Above 12 km of altitude, $n(z)$ is set to zero. The values chosen for the above parameters are taken from Jaenicke (1993). In the context of the present paper, we consider these standard aerosol profiles to be sufficient in order to illustrate our purpose. However, POMEROL allows for including them from independent measurements (e.g. LIDAR) or using an inversion scheme in order to best fit polarization data.

Table 2 shows the top-to-bottom optical depth of the different components of the atmosphere model. These values are computed following Eq. (A.17) to (A.19). For Rayleigh scattering, the optical depth increases with the wavelength as expected. For ozone, the optical depth is negligible for short wavelengths (blue and shorter), but not for the green and orange lines. The aerosol optical depths are presented for the three models described in Table 1. We can observe two behaviors depending on the aerosol size distribution. For the model 1-low with an average size of 0.15 μm, the optical depth increases towards shorter wavelengths. At 620 nm, the value is equal to that of Rayleigh scattering by coincidence. However, as the wavelength shortens, the optical depth of aerosol diverges from Rayleigh scattering as dictated by the Ångström law (Ångström, 1929). For model 2-high and 3-mid, the aerosol optical depth is almost constant over all considered wavelengths, in comparison with Rayleigh or the 1-low aerosol case. This comes from the much larger average size used (0.557 μm).

3.1.5. Topographic map

Our model also incorporates the topography around the instrument. It is used for the computation of occultation: when a light beam hits the ground between the emission and the scattering point, its contribution to the light received by the instrument is set to zero. The topographic altitude data are taken from ALOS GLobal Digital Surface Model AW3D30 DSM of the Japan Aerospace Exploration Agency (Tadono et al., 2016). It has a resolution of 30 m, which can be downgraded to any value in order to reduce the computation time. We use here the highest resolution available. Using this altitude map along with the emission map described above makes the input lights 3-dimensional.

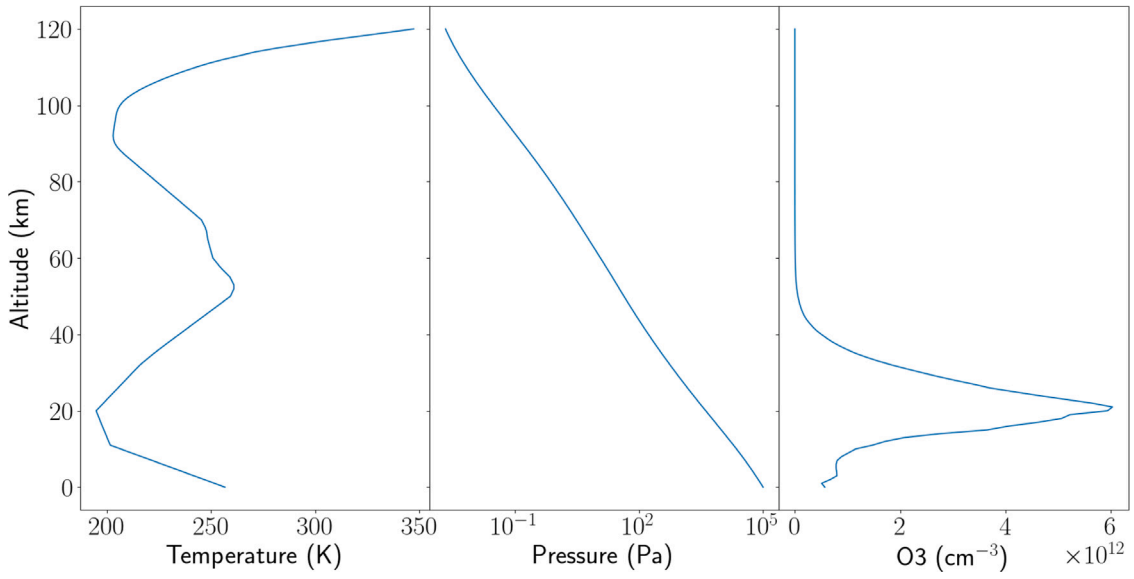

Fig. 2. Mid-Latitude night time atmospheric profiles from the 2001 MIPAS model (see text for details). From left to right: temperature [K], pressure [Pa], Ozone number density [cm^{-3}].

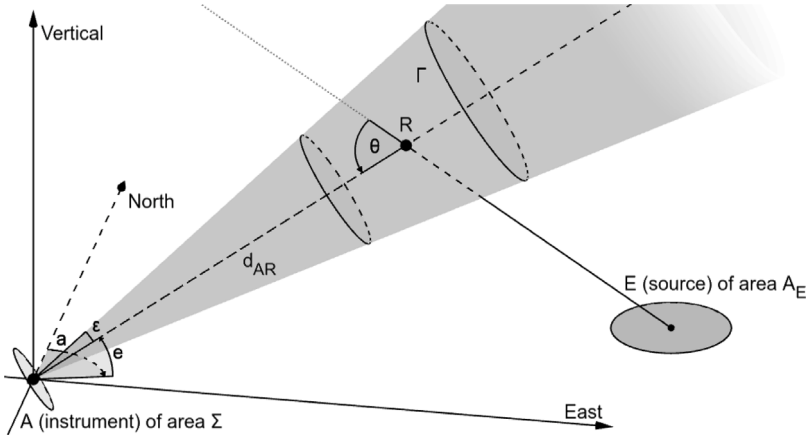

Fig. 3. Geometry of the problem for a light source in E of area A_E, a scattering volume (Γ) centered at R and the instrument in A of area Σ and half aperture angle ϵ. The instrument pointing direction is defined by its azimuth a and elevation e. θ is the scattering angle.

3.2. Radiative transfer model

We describe here the general algorithm used in POMEROL to compute the scattering of extended sources along the line of sight of the virtual instrument. Fig. 4 gives a schematic representation of the process. The two main steps are as follows: the radiative transfer computation and the application of the results to the data. First, the model loads all the necessary input data (see Section 3.1 for details). It then proceeds to compute the light polarization detected by a virtual instrument in this environment. To this purpose, POMEROL is able to compute the polarization of the light coming from any single point source, scattered at any single point along the line of sight and reaching the detector (see Appendix A for details). For one orientation of the instrument, this computation is then repeated $N_{pix} \times N_{los}$ times, where N_{pix} is the number of pixels in the input emission map and N_{los} the number of bins along the line of sight. For this computation, the Stokes parameters are defined with respect to the scattering plane. They are immediately converted to a global reference frame attached to the virtual instrument such that in all of the following steps, all Stokes parameters of every scattering events are defined consistently (see Appendix A.2 for details). This reference frame is defined by the plane containing the line of sight of the instrument and the local vertical. Q is the quantity of vertical and horizontal polarization, while U represents the polarization oriented at 45°. POMEROL integrates all these contributions together to retrieve the total light reaching the detector and its polarization. We call the corresponding Stokes vector $G = (I, Q, U)$. This is computed as the double sum of the Stokes parameters over all point sources and along the whole line of sight as:

$$\begin{cases} I^{total} = \sum\limits_{sources} \sum\limits_{l.o.s.} I \\ Q^{total} = \sum\limits_{sources} \sum\limits_{l.o.s.} Q \\ U^{total} = \sum\limits_{sources} \sum\limits_{l.o.s.} U \ . \end{cases} \tag{8}$$

The units are again given in nW (see Eq. (4)). The integration along the line of sight makes the model pass from its 3D input environment to a 2D map of the polarization properties as a function of elevation and azimuth. Note that every point source scattering contribution along the line of sight used in this sum can be retrieved by the user if needed. One can then use the formulas of Eq. (5) to retrieve the $DoLP$ and $AoLP$ as presented in this article. Then, a uniform, isotropic and constant un-polarized light is added to the result to model the background star

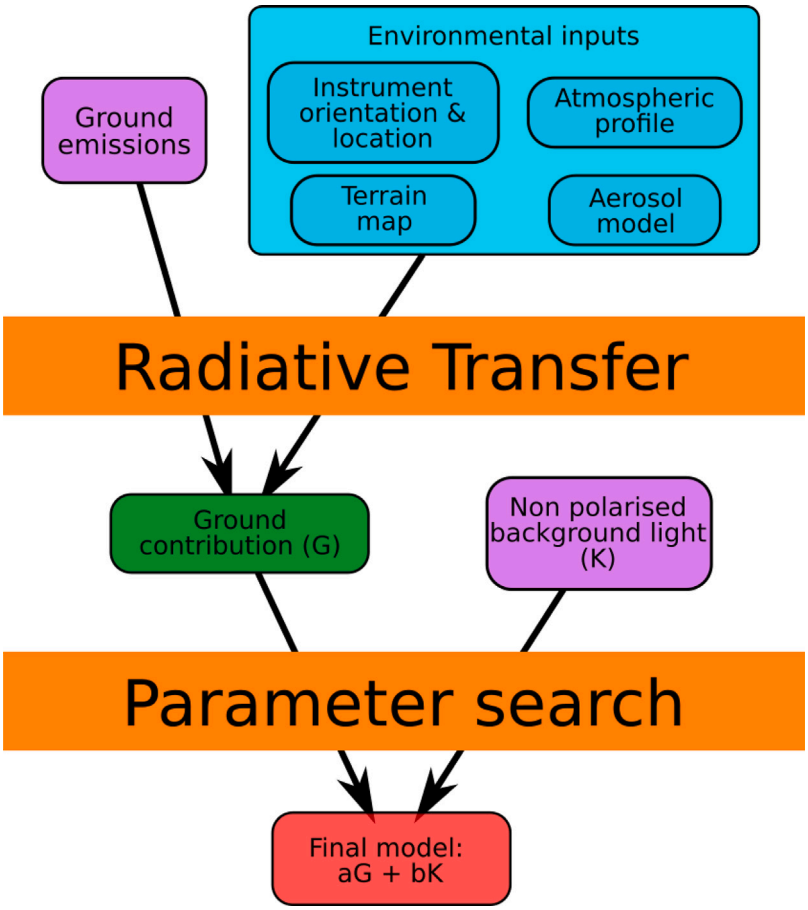

Fig. 4. General overview of the POMEROL algorithm. Environmental inputs (in blue) are described in detail in Section 3.1. In pink, both light sources taken into account in the model: sources on the ground which are detected by the virtual instrument via scattering in the atmosphere (G) and the isotropic un-polarized background (K). The final model is given by a linear combination of both contributions (G and K).

light and the nightglow (K). Both contribution (G and K) are not inter-calibrated, so the final model M is a linear combination of the two: $M = aG + bK$. The parameters of this linear combination (a and b) are chosen to best fit the measurements of the radiant flux (I). The parameter search does not depend at any point on the polarization. Thus, the addition of the background has only two effects. The first one is to inter-calibrate the model units and the instrument units so that the radiant flux is comparable. This step completely determines a and b. The addition of this un-polarized background has a secondary effect, which is to reduce the modeled $DoLP$. We emphasize that the parameter search does not take into account the reduced $DoLP$ and does not try to fit the modeled $DoLP$ to the measurements. Currently, the addition of the background and its renormalization are necessary due to the lack of inter-calibration between our instrument measurements and the input data used for the different emission sources. In the future, the renormalization may be omitted if the required calibrations are available.

4. Model validation and influence of the parameters

In this section we study:

(i) The influence of a localized source on the ground (such as cities), at several distances from the instrument, and in the absence of any source in the sky ;
(ii) The influence of the atmospheric parameters (absorption by O_3, aerosols) for a localized source on the ground;
(iii) The effect of a uniform source in the sky, polarized or not, in the absence of any source on the ground.

These reduced configurations have been chosen so as to illustrate the most important factors that impact ground-based polarization measurements. In the following, we present results by means of clockwise almucantars of elevation 45°, the starting direction being the North. The virtual instrument parameters (Σ and ϵ) correspond to that of the real polarimeter (see Section 3.1.1). In the following series of tests, we use a polarized Lorenz–Mie scattering model for scattering by aerosols (see Section 3.1.4). The comparison between the aerosols models and real data is shown later on in Section 5.1.2. The atmospheric profile used for the tests is the MIPAS standard night-time mid-latitude profile (see Section 3.1). We show here results at $\lambda = 557.7$ nm (auroral green line, Table 3). For the tests presented in this section, an hypothetical source of arbitrary radiance is considered, such that the wavelength only plays a role in computing atmospheric extinction and scattering coefficients. In the following sections where we present comparison with observations, the input emission maps are integrated over the visible spectrum (see Section 3.1.2).

4.1. Influence of a localized source on the ground in absence of any source in the sky

We consider an isotropic point source on the ground of radiance 100 nW/m^2/sr, at different distances d_{AE} away South of the virtual instrument. The purpose of this arbitrary setup is only to showcase the influence of a point source on the ground at different distances from the instrument. Thus, the radiance is arbitrary and does not correspond to any real world values, but the distances are chosen to be representative of a real environment (between 1 and 100 km). There is no mountain obstruction. The ground surface takes the Earth curvature into account.

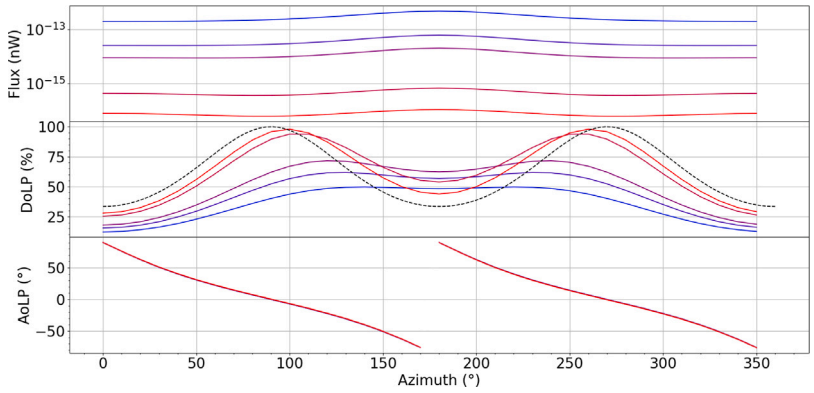

Fig. 5. Almucantar for $e = 45°$, for a point source on ground, on a flat Earth surface, South of the instrument at varying distances d_{AE} (with no aerosols). Upper panel: measured radiant flux [nW] for a source of radiance 100 nW/m^2/sr. Middle panel : $DoLP$ [%]. Lower panel: AoLP [°]. From blue to red: $d_{AE} = 1, 5, 10, 50, 100$ km. In the upper panel, the highest value (in blue) corresponds to the closest source position and the lowest value (in red) to the most distant point source. Similarly, in the middle panel, the most distant point source has two very marked maxima (in red) while the closest is the flattest (in blue). The black dashed line in the middle panel corresponds to a theoretical case for a source at infinite distance.

Only Rayleigh scattering and ozone absorption are taken into account, no aerosols are present in the atmosphere. The ozone is taken into account through its number density vertical profile (Fig. 2) and its absorption cross sections as a function of the wavelength (Fig. A.13). For a source located 100 km away from the observation point, the ozone decreases the measured radiant flux by less than 3%. There is no effect on the $AoLP$ since this angle depends only on the scattering plane (defined by the emission and scattering direction). The effect on the $DoLP$ is smaller than 0.4%, and the closer the source, the lower the effects. More complex sources than a point may slightly increase these values. From now on, we take into account the impact of O_3.

In Fig. 5, we show the polarization results for $d_{AE} = 1, 5, 10, 50$ and 100 km. In all such figures, the upper panel shows the radiant flux measured by the virtual instrument, representing the energy per unit time on the collector, the middle panel shows the $DoLP$ and the lower panel the $AoLP$.

The further the source, the lower the measured radiant flux. However, the effect is not merely a decrease as d_{AE}^{-2}, because the source illuminates points at all altitudes along the line of sight that are integrated on the virtual instrument. Moreover, the light parameters change during its crossing into the atmosphere from the source to the line of sight, and along the line of sight. As seen in Fig. 2, the concentration in ozone peaks at about 20 km. As an example, the decreasing factor between a source lying at 1 and 10 km is about 25 (and not 10^2 if only the effects of the distance were considered). It becomes approximately 5 000 (and not 10^4) with a source at 100 km compared to 1 km. Because of the exponential decrease of the atmospheric pressure with the altitude, this effect is less important when the source moves away from the polarimeter. However, in all cases, the radiant flux is maximum in the Southern direction, i.e. towards the source.

Geometrically, for a single point source and a given line of sight, the $AoLP$ of every scattering point is the same. In this particular case, we do not have to use the I, Q and U notation (Eq. (5)). The total $DoLP$ integrated along the line of sight is an average of the $DoLP(\theta_i)$ of each scattering points i weighted by the scattered radiant flux F_i as

$$DoLP = \frac{\sum_i F_i DoLP_i(\theta_i)}{\sum_i F_i}, \tag{9}$$

where θ_i is the scattering angle at point i, F_i follows Eqs. (A.12) and $DoLP_i$ Eq. (A.20). In the limit of a source infinitely far away from the instrument (on a flat surface), all paths from the source to the instrument are parallel. Thus, the scattering angle is the same everywhere on a given line of sight. The total $DoLP$ measured by the virtual instrument should then follow Eq. (A.20) (dashed line in Fig. 5, middle) since there is no aerosols in this case. When looking eastwards and westwards, the value of the $DoLP$ reaches 100% as expected from the theory. When the source gets closer to the virtual instrument, each point along the line of sight has a different scattering angle, which smooths the variations along the almucantar. On a flat surface, the $AoLP$ is the same whatever the distance from the source (Fig. 5, bottom).

4.2. Influence of the aerosols for a localized source on the ground

The aerosols are taken into account through their number density vertical profiles and their cross sections (Table 1). The aerosol cross section depends on the wavelength as computed using Lorenz–Mie theory (Lorenz, 1890; Mie, 1908; Born and Wolf, 1999). For the sake of simplicity, we consider the aerosol refractive index to be the same for all wavelengths. A variation of the refractive index with wavelength could be taken into account, but is out of the scope of the present study.

In order to illustrate the effect of the aerosols, we consider again the three different profiles listed in Table 1: 1-low, 2-high, 3-mid. The impact of the aerosol profiles is drastic, but not straightforward to interpret. It is illustrated in Fig. 6, for a point source located 5 km South from the observation point. With the 1-low model (lowest aerosol contribution), the radiant flux is increased by 600% (with respect to the case with no aerosols) when pointing above the source, and by 40% in the opposite direction. Using the 2-high profile (highest aerosols contribution), the radiant flux is increased by 150% when pointing above the source, and decreased by 40% in the opposite direction. With the 2-mid model, the radiant flux above the source increases by 120%, against 10% in the opposite direction. The ratio of the maximum to minimum radiant flux along the almucantar is in all cases amplified by the presence of aerosols.

For an increasing aerosol contribution, the $DoLP$ decreases in the direction of the source. With the 1-low model, it decreases by about 50%, with the two maxima along the almucantar still present. The $AoLP$ does not change since the aerosol radius is small compared to the wavelength, and the polarization direction is the same as for Rayleigh scattering ($AoLP^{ray}$). However, when the aerosol size is large compared to the wavelength (2-high and 3-mid), the $DoLP$ behavior changes drastically, with a maximum at about 25% when pointing away from the source. The $AoLP$ is shifted by 90° when pointing away from the source due to larger aerosol size, while it is the same as $AoLP^{ray}$ when pointing towards the source. The impact of aerosols on the virtual instrument observations is complex. They may for instance either increase or decrease the intensity depending on their size or on the scattering angle. They do therefore play a major role. Spanning all possible aerosol models is not the main goal of the present study, and we limit ourselves to the three models presented here.

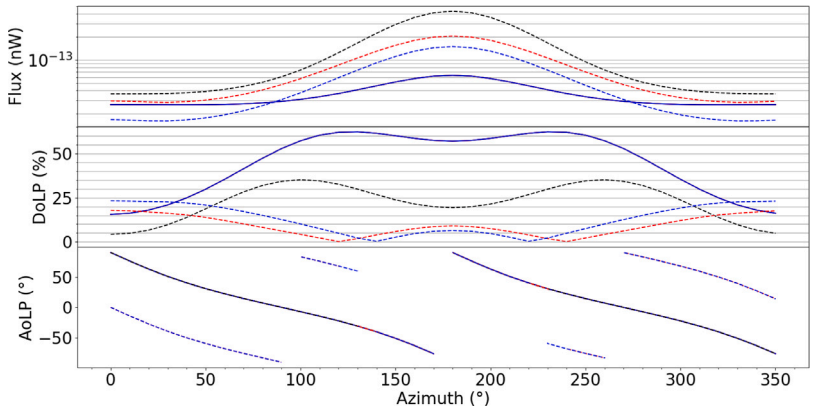

Fig. 6. Almucantar for $e = 45°$, for different aerosol profiles. A point source is located 5 km South of the instrument. The continuous line is the case without aerosols (similar to Fig. 5). The dashed lines correspond to three different aerosol models listed in Table 1: 1-low (black), 2-high (blue) and 3-mid (red).

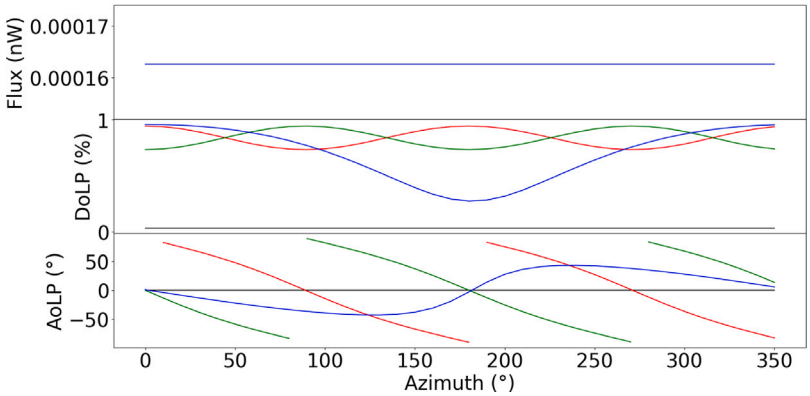

Fig. 7. Polarization parameters for an almucantar at $e = 45°$ in the presence of an isotropic skylight of radiance taken at 100 nW/m^2/sr at 557.7 nm. No aerosols are present in the model. The direct radiant flux is taken into account, with different polarization parameters. No polarization of the skylights (black line), with a 1% polarization along the East–West (red) and North–South (green) directions, and along the magnetic field direction (blue).

4.3. Influence of the skylight with different polarization parameters

We document here the effect of a simple skylight (nightglow and/or integrated star light). It is modeled as an infinitely thin uniform sky emission of arbitrary intensity at 110 km of altitude. The model computes the sum of the non scattered light and the single Rayleigh scattered light measured by the instrument. In order to prepare for further auroral studies (out of the scope of this article), we allow this emission to be polarized (Bommier et al., 2011). Fig. 7 shows the model outputs over an almucantar (with no aerosols), for a nightglow either unpolarized, or polarized with a $DoLP = p_{source} = 1\%$ (arbitrary choice) along several directions: East–West (EW), North–South (NS) or along the magnetic field (B). For this last case, the instrument is positioned at latitude 45.2123°N and longitude 5.9369°E and we use the CHAOS-6 internal magnetic field model (Finlay et al., 2016) evaluated in 2019. The atmospheric profile described in Section 3.1 is used. As the background skylight is isotropic, the measured radiant flux does not change over an almucantar.

In cases where the nightglow is polarized at the origin, the $DoLP$ depends on the angle α between the line of sight and the polarization direction, as $DoLP = p_0 + p_1 \sin\alpha$. For the EW and NS cases, $p_0 \approx 0.85 p_{source}$ and $p_1 \approx 0.1 p_{source}$. When the nightglow is polarized along the magnetic field lines, the behavior is much different as the lines are close to vertical, with $p_0 \approx 0.6 p_{source}$ and $p_1 \approx 0.3 p_{source}$. For a uniform sky emission and in the absence of other sources, Fig. 7 shows that the polarization from Rayleigh scattering in the atmosphere is relatively small compared to the polarization of the non scattered light. Thus, in this simple configuration, any polarized source in the sky with a $DoLP$ higher than the instrument noise level should be detectable.

The $AoLP$ (lower panel) for the unpolarized nightglow emission (continuous black line) is undefined (it is set to zero by default, with no physical meaning). The EW and NS cases show an $AoLP$ regularly rotating over all 360° with the same behavior, but shifted in azimuth by 90°. As expected from the $DoLP$ definition, the maximum $DoLP$ corresponds to a 90° $AoLP$. When the nightglow polarization direction is aligned along the magnetic field, the magnitude of the $AoLP$ variations along an almucantar is significantly weaker, within ±40°, which led (Bosse et al., 2020) to reject this single source as the origin of the measured polarization of auroral lights.

5. Comparison with geophysical measurements at mid-latitude

In order to validate our model, we performed a series of observations in the French Alps. In the following, we focus on the night from the 19th to 20th of January, 2021 when the Moon was down (below −10° elevation during the whole observation). The latitude is 45.2123° and longitude 5.9369°. The altitude is 770 m. The nearest city is Grenoble 15 km away with downtown at an azimuth of 260°. However, the valleys around this bright city produce also some light pollution. Fig. 1 shows the geographical configuration with lines of constant elevation at 500 m, 1000 m and 2000 m.

The light pollution was clearly visible with the naked eyes. At the time of the observations, the snow was covering the ground above about 500 m elevation. The altitudes below $h \approx 1500$ m are mostly covered with forests in the mountains which lowers the albedo significantly, even though some snow remains on the trees. The air temperature was below 0 °C all over the surrounding area, and reached about −5 °C at the point of observation. The modeling below takes

Table 3
List of emission lines observed during the January, 2021 campaign (see text). All emissions are present in the light pollution spectrum.

Name	Wavelength (nm)	Instrumental width (nm)	Atmospheric source	Layer
Orange	620	2	OH	High Mesosphere (< 80 km)
Green	557.7	10	O	Thermosphere (110 km)
Blue	427.8	10	N_2^+	Ionosphere (90 km)
Purple	391.4	10	N_2^+	Ionosphere (85 km)

the relief into account (see Section 3.1). We could observe simultaneously four wavelengths, summarized in Table 3: three of them concern emissions bands emitted in the upper atmosphere, either in the thermosphere (green, due to the O^{1S} excitation state) or in the thermosphere (blue and purple, due to the 1^{st} N_2^+ negative band). The "orange" band around 620 nm is not present in the thermosphere, but is emitted in the mesosphere by OH(5–0) and OH(9–3), though with a relatively lower radiant flux (Broadfoot and Kendall, 1968; Bellisario et al., 2014, 2020).

We show below the results of an almucantar at a constant elevation $e = 45°$ from 1:18 UT to 3:35 UT taken with the real instruments and compared to the virtual one (i.e. the modeling). We rotate clockwise from North to the East and back to North with 10° increments in azimuth. At each step in azimuth, we record the radiant flux, $DoLP$ and $AoLP$ during about one minute and 30 s. We recall that our instrument provides the relative (uncalibrated) measurements of the radiant flux, and the calibrated $DoLP$ and $AoLP$. The orientation angles e and a are set using stars as references, together with a compass (to help on the increments in azimuth) and an inclinometer (for the elevation). We consider the accuracy to be of the order of ±2°.

We focus first on a single wavelength (the green line, see Section 5.1) for which we detail our analysis of the observations. We next discuss the full picture in Section 5.2.

5.1. Model predictions versus observations in the green line

Fig. 8 shows an almucantar in the green line. The radiant flux maximizes above downtown Grenoble ($a = 260°$, this is clearer in Fig. 10). In the theoretical case of a point source, the $DoLP$ maximizes at ±90° of the direction of this point (see Section 4 and Fig. 5). Here, the $DoLP$ shows a single maximum near 240° in azimuth, illustrating the influence of an extended pollution source. The value of its measured maximum is around 12%. The $AoLP$ rotates regularly with a behavior very similar to that of a point source on the ground westward with respect to the instrument.

5.1.1. Modeling without accounting for aerosols and background skylight

We first run our POMEROL model with the light pollution as single input (i.e. with neither aerosol nor natural background skylight). We use a ground emission map composed of 1000 pixels mapping an area of 100 km radius around the instrument. The elevation map covering the same area is used to model the mountain obstructions, with a 30 m resolution. We recall that the emission maps are not intercalibrated with our instrument, so that the units for the radiant fluxes are arbitrary. The ozone is taken into account, although its effect remains small. The results are shown in Fig. 8 (black stars). Both the modeled and measured radiant fluxes peak around the same azimuth (260°). However, the radiant flux variations along one almucantar are significantly larger for the model: the maximum radiant flux is 110% higher than the minimum for the model, with respect to only 43% for the measurement.

The modeled $DoLP$ reaches 47% at its maximum around 200° azimuth, about 4 times higher than the highest measured $DoLP$, and is offset by 40° in azimuth. A second local maximum at 300° azimuth is also present in the model, and absent from the measurements. Two maxima in the $DoLP$ are indeed expected for a point source (see Fig. 5) and are due to the scattering in the first few kilometers of atmosphere. Here it is smoothed out because of the multiple light sources and the occultation from the mountains. This feature is not present in the data and may hint that the model overestimates the scattering below 10 km.

The modeled $AoLP$ is very similar to the measurement, showing the same rotation pattern at almost the same angles, except around 90° in azimuth (i.e. pointing away from Grenoble). This difference can be explained by the poor quality of the data in this direction where the radiant flux is minimal and the $DoLP$ close to zero, inducing large uncertainties on the $AoLP$ measurements (see Bosse et al., 2020).

This first simple approach does not take into account one or more additional sources. We will now show the effects of introducing either a natural background light or the aerosols.

5.1.2. Impacts of background skylight and aerosols

The fact that the model overestimates the radiant flux variations and the $DoLP$ in the case above is an indication that non-polarized (or little-polarized) additional sources must be taken into account. Such sources exist naturally: they are the nightglow and the integrated star light. This behavior can also be due to the lack of multiple scattering in the model (Hovenier, 1971; Pust and Shaw, 2011). The exact contributions of those sources is delicate to evaluate at this point, so we fit them together as the *background skylight* in such a way that the variation's amplitude of the modeled radiant flux match the measured one. This method constitutes therefore an indirect estimate of this background skylight (see red + in Fig. 8). Here, it is considered constant, isotropic and unpolarized (these approximations could be reconsidered in the future by estimating each contribution from independent measurements or more accurate models, see Section 3.1.3). Averaged over an almucantar, this results in approximately doubling the total radiant flux received by the instrument. This is not visible in Fig. 8 because of the Arbitrary Unit radiant flux scale. As expected, the $DoLP$ is decreased in any direction by about 50%, peaking at 25% around 220° in azimuth. The two maxima in the modeled $DoLP$ over one almucantar are still present, although the secondary maximum appears attenuated. The $AoLP$ is unchanged in comparison with the previous case with no background sky, which is expected since the natural background is not polarized.

We now turn to a case with no background skylight, but with the aerosol polarized models included (see Section 3.1.4). The amplitude of the modeled radiant flux variation along the almucantar become larger, whatever the aerosol model, as seen with the synthetic case in Fig. 6. The higher the aerosol contribution, the higher the radiant flux variations. The modeled $DoLP$ decreases when the aerosol contribution increases, so that it is possible to find a model (2-high: magenta ϒ) that matches the measured $DoLP$. However, this makes the modeled $AoLP$ depart from the measurements, so that it is not possible to find a set of aerosol parameters that allows fitting the measured radiant flux, $AoLP$ and $DoLP$ at once.

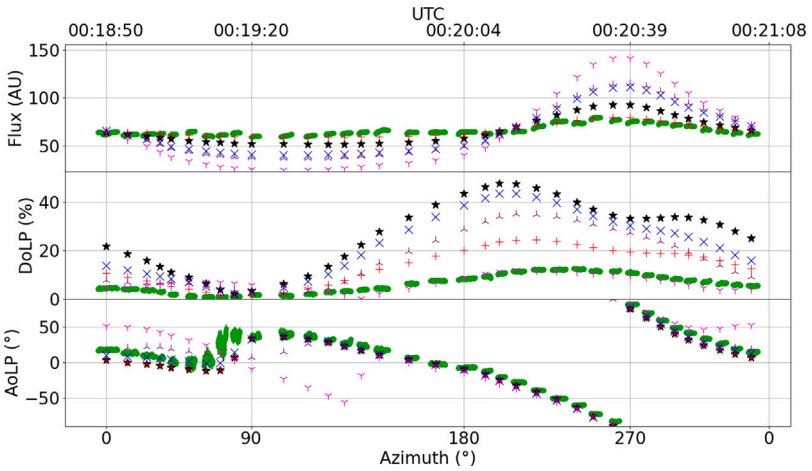

Fig. 8. Comparison between model outputs and observational data. Measured data are shown in green, the width of the lines indicating the errorbars (for their computation, we refer to Bosse et al., 2020). Errors on the azimuth due to the pointing direction are of the order of a few degrees (not shown). The other symbols indicate the model output for a ground light pollution map (see text for details). Several aerosol profiles are considered. (see Table 1): without aerosols nor background lights (black ★); without aerosols and with background lights adjusted to fit the radiant flux variations (red +); without background lights and with aerosols model 1-low (blue ×), 2-high (magenta ϒ) and 3-mid (purple ⅄). Abscissa are given as the pointing direction under the bottom panel (azimuth where 0 is North, 90 is East) and the corresponding time in UTC format above the top panel.

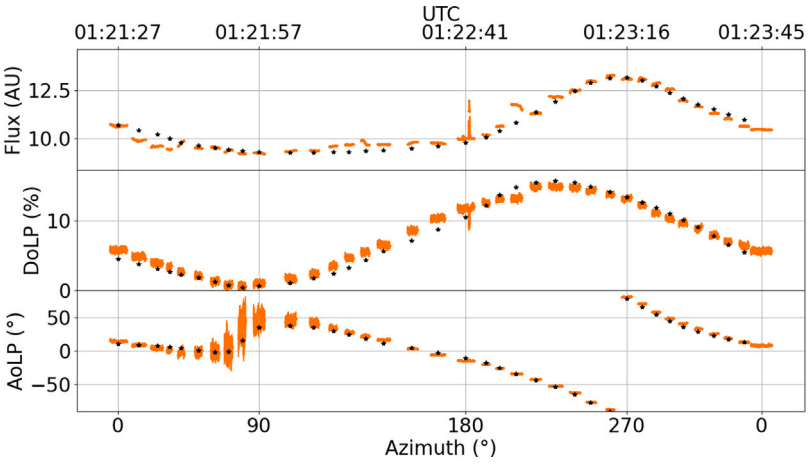

Fig. 9. Almucantar in the orange line (620 nm). Measured data are shown in orange, the width of the lines indicating the errorbars. Errors on the azimuth due to the pointing direction are of the order of a few degrees (not shown). Model predictions (black stars) are obtained with the 1-low aerosol profile plus an unpolarized, isotropic background skylight adjusted so as to fit the radiant flux (see text).

5.2. Comparison of the observations and the modeling in four wavelengths

From the results presented above, we deduce that even though both additional sources (background and aerosols) significantly affect the polarization parameters, none of them reproduce the measurements alone. We consider below the model predictions for a combination of those two contributions. We first have to choose an aerosol profile. We use the 1-low aerosol model, as it fits best the measurements when combining with background skylight. It could already be intuited from Fig. 8 as the 1-low profile affects less the $AoLP$ than the other ones. This choice is also coherent as we observe in the Alps at an altitude where the air is very clean. We show hereafter model outputs with this aerosol profile together with a natural background skylight. At all wavelengths, the modeled radiant flux is the highest in the direction of the city of Grenoble, and the model predictions for the $AoLP$ convincingly fit the observed values (see Figs. 10 to 12).

Examination of Fig. 8 shows that, without any contribution from the background or aerosols, significantly larger values of the $DoLP$ are modeled in the green line (557.7 nm). The blue (427 nm) and the orange lines (620 nm) behave similarly. For these three wavelengths, the measured radiant fluxes are fitted when adding the 1-low aerosol model and respectively 114% (Fig. 10), 213% (Fig. 11) and 43% (Fig. 9) of natural background radiant flux (integrated star light and/or nightglow). The percentages are calculated with respect to the maximum radiant flux measured by the instrument around azimuth $a = 260°$. Absolute values are irrelevant here, since we do not know the spectral emissions of the input maps and the instrument is not calibrated. Interestingly, for these three colors we now reproduce also the minima and maxima of the observed $DoLP$ along one almucantar, without adding any further complexity to the model. If slight discrepancies remain for the shape of $DoLP(a)$ between the model and measurements for the blue line, this characteristic is very convincingly reproduced by the model in the green and orange lines.

It is striking that we manage to replicate these observations with our model in three different wavelengths simultaneously, as they are affected differently by light pollution, the natural background from the sky, and multiple scattering. Indeed, there exist some orange emissions in the star light and in the mesospheric nightglow (Bellisario et al., 2014, 2020). The green and the blue lines exist both in the stellar light and the natural nightglow originating in thermospheric and/or ionospheric emissions. The orange is the tiniest of the three (Broadfoot and Kendall, 1968). The blue in the urban light spectrum is much dimmer than the green or the orange. These considerations are compatible with our results.

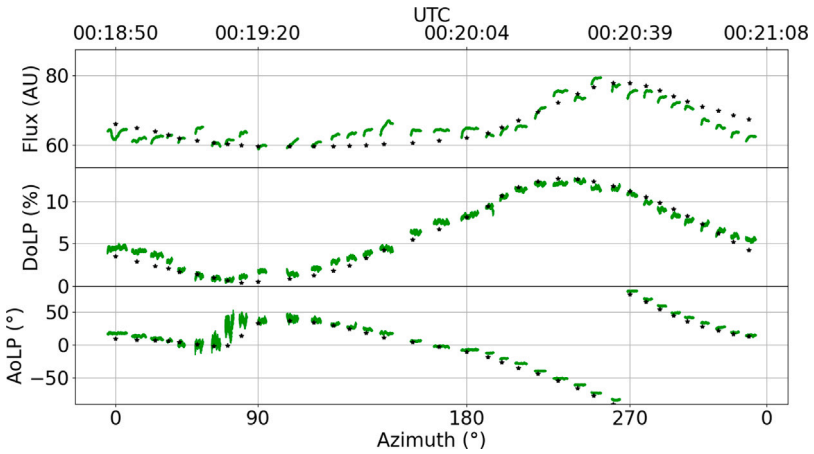

Fig. 10. Same as Fig. 9 for the green line.

Finally, the misfit in the $DoLP$ observed for the purple line can have several sources. First, it might require an adjusted aerosol profile (see e.g. Figure 3 in Bergstrom et al., 2003). For example a different size distribution which would influence differently the shorter and the longer wavelengths. This would demand a thorough study of aerosol contribution, which is out of the scope of this paper. Furthermore, this difference in $DoLP$ is likely related to the stronger impact of MS towards short wavelengths. The effect of multiple scattering has several consequences on the behavior of the radiant flux measured along the almucantar, and on the $DoLP$. Multiple scattering increases the scattered radiant flux, and decreases the $DoLP$. At shorter wavelengths (blue and purple in our case), this effect can decrease the $DoLP$ as much as 20% to 30%. At longer wavelengths (orange, green), the discrepancy is lower (Staude, 1975; Ugolnikov et al., 2004). The effect of multiple scattering on the radiant flux cannot be modeled easily using a linear coefficient (Hansen, 1971). A proper implementation of MS is out of scope of this paper, but is in development phase. We note that the two main effects of MS are very similar to the effects of our background light, which also increases the radiant flux and decreases the $DoLP$. Of course, such a simple isotropic source cannot reproduce the complexity of MS. But it is possible that in its current state, the model tends to overestimate the background radiation of skylight and airglow to compensate for the lack of MS. A third possible cause of the discrepancies observed at short wavelength is the input emission map used by the model. Indeed, the magnitude of the signal from the ground is likely very small in the purple (391.4 nm), because in this wavelength the radiant flux of city lights is on average very weak (see for instance the spectral analysis of Fig. 6 in Bosse et al. (2020) and references herein). Therefore, the emission map of the model which integrates all the visible spectrum might not represent the actual emission geometry at short wavelengths. For example, if a city has switched to LED street lamps (shorter wavelength), or still uses more reddish lighting, it relative contribution to the emission geometry will change depending on the wavelength. The very low radiant flux measured by the instrument in the purple line means that the $DoLP$ has large error bars. This in turn also affects the uncertainty level for the $AoLP$. The changes of the $DoLPs$ with the azimuth appear rather flat, but is also less tightly constrained. All these sources of errors (no MS, aerosol size distribution, spectral variation of the emission map and large uncertainties on the data) can easily explain why the model fails at predicting the low values of the $DoLP$ observed in the direction of Grenoble at short wavelengths.

6. Discussion

We have presented in this study a polarized radiative transfer model in the single scattering approximation, which can account for a spread light pollution from the ground (including the surrounding topography), natural skylights (from stars or the nightglow) and the effect of aerosols. To our knowledge, it is the first time that such a radiative transfer code is derived in order to answer the question of the nightlight polarization, even though radiance models already exist (Falchi et al., 2016; Hänel et al., 2018; Wang et al., 2020). We have confronted this model to measurements performed at mid-latitudes in the French Alps in four different wavelengths, either within or outside the lines of emissions for the natural nightglow. We obtain a convincing comparison between the model outputs and the observations of the relative radiant flux, degree and angle of the linear polarization in the three wavelengths with the highest signal-to-noise ratio (green, orange and blue lines).

The results presented in this paper show the feasibility of nocturnal polarization measurements and modelization. Our model, although currently limited to a single scattering scheme, is doomed to evolve, and constitutes a proof of concept that paves the way to further investigations of the night-sky light polarization.

Our results show that several contributions must be considered in order to explain observations: extended sources on the ground (light pollution from the nearby cities) and an isotropic source in the sky (the background via starlight and nightglow, plus a possible correction for multiple scattering). Of course, the atmospheric model must include Rayleigh scattering and Lorenz–Mie scattering by aerosols. We discuss below several potential applications of this model.

First, it can be used to interpret properties of the polarized lights measured at high latitudes under auroral conditions. This was the main purpose for its development. The first attempt at confronting model predictions and auroral observations tends to validate a polarization near the source of emissions in the ionosphere (Bosse et al., 2022a). The preferred mechanism favors an orientation of the polarization influenced by electrical currents, instead of magnetic field lines as initially proposed by Lilensten et al. (2016). The present study shows that the use of wavelengths outside the ionospheric emissions lines is crucial to determine a correct profile of aerosols, as this latter is of prime importance to understand the measured radiant flux and $DoLP$. Furthermore, in auroral conditions, ionospheric lights will strongly dominate over the integrated starlight. As a consequence, the complex picture of these emissions (2D maps) is needed as an entry of the model. Moreover, in countries where wide areas are covered with snow, the reflection of auroras on the ground might be of importance. This added complexity is fully described in Bosse et al. (2022a) as it is specific to auroral studies. We have also shown that our code can handle a polarized background source such as polarized airglow. Its signature (if any) should be detectable despite the Rayleigh and Lorenz–Mie scattering. We have shown that a horizontally polarized uniform sky source produces $AoLP$ changes along an almucantar that resemble to

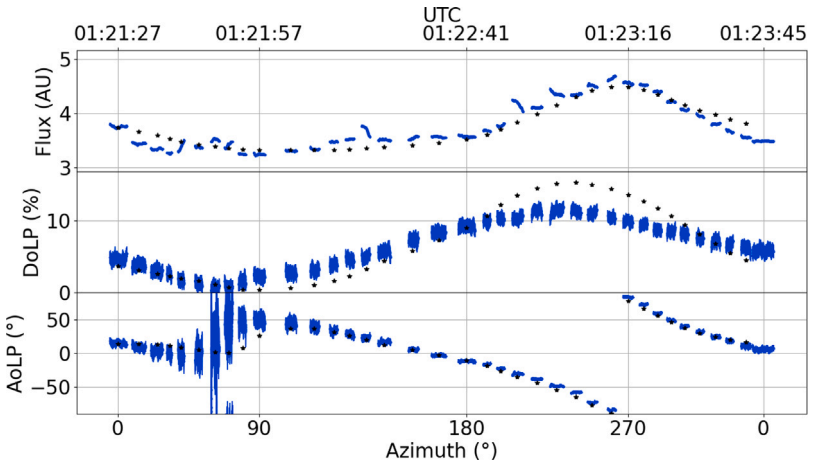

Fig. 11. Same as Fig. 9 for the blue line.

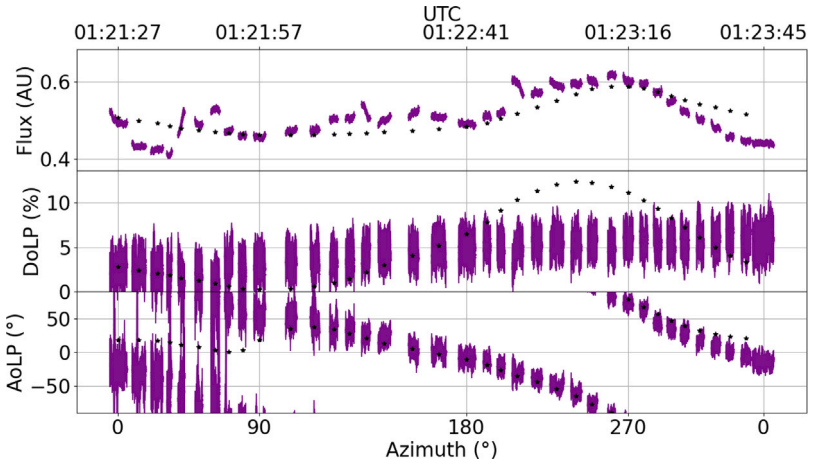

Fig. 12. Same as Fig. 9 for the purple line.

the ones produced by scattering within the atmosphere. It resonates with the possible polarization by horizontal ionospheric currents (Bosse et al., 2022a,b). These can be partially reconstructed from ground-based magnetometers (e.g. Amm and Viljanen, 1999; Pulkkinen et al., 2003). This possibility is motivated by the observation of coherent fluctuations in time series for both the polarization parameters of auroral lights, and the electron density content in the ionosphere (Bosse et al., 2020) as well as by the study of polarized blue and purple emissions in a laboratory experiment (Bourgeois et al., 2022). This may have further consequences for the study of the equatorial airglow, below the electrojet.

We have shown that the relative contribution of background lights to scattering strongly varies with the wavelength: from +43% for the longest one (orange), to +114% in the green and +219% in the shortest one (blue). Measuring how much this means in absolute units would require the knowledge of the city light spectrum (that is not provided with the input maps) as well as the instrument transfer function (such a calibration would require a dedicated study, as it depends on the photo-sensors and on the opacity of the filters used in the instrument). This higher background contribution at shorter wavelengths can be a sign that the background partly corrects the effect of multiple scattering, since its contribution is expected to be higher at short wavelengths. This result is also compatible with the expected relative contributions from the city lamps, the nightglow and the starlight. On the one hand, the city contribution is likely higher in the green and orange than in the blue, as LED lights are in minority in the region. This means that the same sky emission for all three lines should lead to a relatively higher contribution of the background for the blue. On the other hand, if we were to detect a contribution from the nightglow, we would expect relatively higher radiant fluxes in the blue and green than in the orange (which is not emitted in the ionosphere), for a constant contribution of the cities at the observation point. Thus our results are fully compatible with the nightglow emissions, showing that the method may be used for such studies. Moreover, adjusting the modeling to the observations requires a contribution from the integrated starlight (at least that for the orange). The combined contributions of the nightglow and the starlights can therefore be detected with this method even in the presence of light pollution, although we cannot distinguish yet between the two sources.

Another major result is the influence of the aerosols. Several techniques are already used for aerosols studies using scattering of the Sun or night-time lights (Tomasko et al., 2009; Hasekamp, 2010; Snik et al., 2014; Wang et al., 2016; Zhou et al., 2021). Our model could extend such applications to night times, improving upon the study by Wang et al. (2020) of unpolarized night lights. The good fit between the model and the measurements at several wavelengths comes with a determination of the size distribution, profile distribution and refractive index of the aerosols. Any attempt to change drastically these parameters degrades the fit. The precise determination of the aerosol parameters is out of scope of this preliminary study. It would require for example using independent measurements (such as LIDAR) or dedicated inversion schemes in order to optimize the input model parameters. Nevertheless, we have shown that the measurement of the light polarization constitutes an original way for aerosol studies

at night. This potential application could be used in the future after careful calibration of the model for this goal and the addition of multiple scattering. As of today, this article only presents the inner working of the model in view of future use by other interested teams.

We can think of other uses for study and monitoring of light pollution impact on the environment which require less precision than aerosol retrieval. In this context, POMEROL could be used to approximate the night sky polarization in urban and rural areas, under different conditions, in the presence or not of the Moon light, in the middle of the city or in the suburbs, etc. We believe that our model could be helpful for future studies, even with its current limitations, the first of which being the omission of multiple scattering. This should be implemented in future versions for a better concordance with observations. Different methods could be used to incorporate multiple scattering in POMEROL, such as forward or backward Monte Carlo approaches (Ramella-Roman et al., 2005; Yong et al., 2016), doubling adding method (Hovenier, 1971) or path integrals (Petržala, 2021). Even though this work is out of the scope of this paper, we anticipate that a reversed Monte-Carlo approach is particularly adapted to our model since the light sources are spread and the detector is small. This could save significant computation time but introduces difficulties for polarization tracing. We have shown that the impact of multiple scattering can be partly counter balanced via the unpolarized isotropic background for the blue and longer wavelengths, without ruling out our model. Furthermore, pollution maps are not provided for all wavelengths (but these might be calibrated with in situ measurements). Finally, although we found that an isotropic sky was enough to fit our observations in the green and orange lines, a more complex model of starlight and nightglow that takes into account variations in time and space could further improve the model. Our study paves the way to future investigations of the night-light polarization, and calls for dedicated evolution of the model.

Nevertheless, our results suggest that our single-scattering polarized radiative transfer model together with our polarimeter may be used during night-time to detect light pollution even in remote areas, and to diagnose the aerosol content with for instance potential applications concerning air quality. The experimental technique is passive, contrary to lidars, low power consumption (less than 5 W), easily transportable in a suitcase, and can use any kind of visible source (artificial or natural such as the Moon, the skylight, the airglow). These polarimeters may be deployed over a large area, thus allowing in the future a global coverage.

CRediT authorship contribution statement

Léo Bosse: Conducted all observations, Wrote the code of POMEROL with the help of OP, CB, JL and NG, Ran all the simulations, Results analysis and interpretation, Wrote the manuscript, Redacted the manuscript. **Jean Lilensten:** Lead, Conducted all observations, Built and developed all observations, Results analysis and interpretation, Wrote the manuscript, Redacted the manuscript. **Nicolas Gillet:** Conducted all observations, Results analysis and interpretation, Wrote the manuscript, Redacted the manuscript. **Colette Brogniez:** Results analysis and interpretation, Wrote the manuscript, Redacted the manuscript. **Olivier Pujol:** Results analysis and interpretation, Wrote the manuscript, Redacted the manuscript. **Sylvain Rochat:** Built and developed all observations, Redacted the manuscript. **Alain Delboulbé:** Built and developed all observations, Redacted the manuscript. **Stéphane Curaba:** Built and developed all observations, Redacted the manuscript. **Magnar G. Johnsen:** Insight and ideas, Supplied the infrastructure necessary for auroral light observations campaigns, Redacted the manuscript.

Declaration of competing interest

The authors declare that they have no known competing financial interests or personal relationships that could have appeared to influence the work reported in this paper.

Data availability

The source code of the POMEROL model is made freely available by the authors here: https://github.com/LeoBosse/analysis/tree/master/pomerol.

Ground emission maps from the NOAA Earth Observations Group (Elvidge et al., 2013) are available here: https://eogdata.mines.edu/products/vnl/.

Atmospheric profiles from the 2001 MIPAS Model Atmospheres (Remedios et al., 2007) are available here: http://eodg.atm.ox.ac.uk/RFM/atm/.

Elevation data from the ALOS GLobal Digital Surface Model AW3D30 DSM of the Japan Aerospace Exploration Agency (Tadono et al., 2016) are available here: https://www.eorc.jaxa.jp/ALOS/en/index_e.htm.

Acknowledgments

This work was partly funded by the French polar institute IPEV under program POLARLIS 3, number 1026. It was also funded by the Prematuration CNRS program and by the Maturation program CM180023, project PTCU Number 180018M from the SATT company Linksium. The polarimeter is patented by the CNRS and valorized by Linksium (international patent number 1873378). We thank the Programme National Soleil-Terre for its financial support. We thank Pierre Simoneau (ONERA) for useful discussions on the mesospheric nightglow.

Appendix A. Computation of the radiant flux measured by our virtual instrument

A.1. Computation of the radiant flux measured by the virtual instrument

In this appendix, we compute the radiant flux measured by a virtual instrument in A when the light is emitted by a single point source E, and scattered at a single point R along the line of sight (see Fig. 3). We describe each intermediate step in order for the reader to understand and reproduce our results.

We use here the units used by POMEROL, with the scale factor implemented in the code. The scale factor has no effect on the dimensional analysis, but are kept here for more transparency on the code.

First, the source is fully described by its radiance L_E in nW/m^2/sr as given by the input map (see Section 3.1), and its surface area A_E in m^2. It is considered small enough to be approximated as a point source of radiant intensity $I_E = L_E A_E$ in nW/sr. Its emission is considered isotropic. From this, the irradiance E_E reaching the scattering volume in R is (in nW/m^2)

$$E_E = L_E \Omega_E \exp(-\tau_{ER}) = L_E \frac{A_E}{d_{ER}^2} \exp(-\tau_{ER}), \tag{A.1}$$

where $\Omega_E = A_E/d_{ER}^2$ is the solid angle of the emission surface as seen from the scattering point at a distance d_{ER} (in m), and τ_{ER} is the effective optical depth of the atmosphere between the emission in E and the scattering volume Γ in R (see Eq. (A.16) to (A.19)).

The radiant intensity I_R (in nW/sr) scattered by the volume of atmosphere Γ around R is

$$I_R = E_E \sigma \frac{\Phi(\theta)}{4\pi}, \tag{A.2}$$

where σ (in m^2) is the total scattering cross-section of the molecules or particles, θ is the scattering angle and $\Phi(\theta)$ is the scattering phase function (see Eq. (A.4) and following text). By definition the phase function Φ is dimensionless and normalized across a sphere (e.g. Mishchenko et al. (2002), Chandrasekhar (1960)), such that:

$$1 = \frac{1}{2}\int_{\theta=0}^{\pi} \Phi(\theta)\,\sin(\theta) d\theta \tag{A.3}$$

It ensues that $\Phi(\theta)/(4\pi)$ has units of sr^{-1}. The phase function Φ and total scattering cross-section σ to consider is different whether we consider Rayleigh scattering on air molecules or Lorenz–Mie scattering on aerosols.

$$\Phi_{ray}(\theta) = \frac{3}{4}\left(1+\cos^2\theta\right) \tag{A.4}$$

is the Rayleigh phase function (Bucholtz, 1995). It does not take into account molecular anisotropy effects. This approximation does not affect our results significantly, but could be improved in the future if necessary using a formula from Chandrasekhar (1960). The aerosol phase function $\Phi_{aer}(\theta)$ is computed using Lorenz–Mie scattering theory (Lorenz, 1890; Mie, 1908; Born and Wolf, 1999) and depends on the aerosol model parameters listed in Table 1. For the air molecules, the scattering cross-section is

$$\sigma_{ray} = \beta\,\Gamma\,, \tag{A.5}$$

while for aerosols it is

$$\sigma_{aer} = \bar{\omega} C_{ext}\,\Gamma\,, \tag{A.6}$$

with β the Rayleigh scattering coefficient in m^{-1} as described in Bucholtz (1995) (see Eq. (A.13) to (A.15)), $\bar{\omega}$ the single scattering albedo of the aerosol, C_{ext} the extinction coefficient of the aerosol in m^{-1} and Γ the scattering volume centered around R in m^3. Γ, the scattering volume (see Fig. 3), is a truncated cone defined by ϵ the half aperture angle of the virtual instrument (similar to that of the real polarimeter), d_{AR} and l the height of the cone. It is given by

$$\Gamma = \frac{\pi}{3}\tan^2(\epsilon)\; l\;\left(3d_{AR}^2 + l^2/4\right)\,. \tag{A.7}$$

Finally, the radiant flux in nW measured by the virtual instrument in A is

$$F_A = I_R \Omega_A \exp(-\tau_{AR}) = \frac{I_R \Sigma}{d_{AR}^2}\exp(-\tau_{AR})\,, \tag{A.8}$$

where Ω_A is the solid angle (in sr) of the detector as seen from the scattering volume in R, Σ is the surface area of the detector (in m^2), d_{AR} is the distance from the scattering point to the detector (in m) and τ_{AR} is the effective optical depth along the path from R to A. Developing I_R into the initial parameters gives us:

$$\begin{aligned} F_A &= I_R \frac{\Sigma}{d_{AR}^2}\exp(-\tau_{AR}) \\ &= E_E \sigma \frac{\Phi(\theta)}{4\pi}\frac{\Sigma}{d_{AR}^2}\exp(-\tau_{AR}) \\ &= L_E \frac{A_E}{d_{ER}^2}\exp(-\tau_{ER}-\tau_{AR})\sigma\frac{\Phi(\theta)}{4\pi}\frac{\Sigma}{d_{AR}^2} \\ &= \frac{L_E}{4\pi}\frac{A_E}{d_{ER}^2}\frac{\Sigma}{d_{AR}^2}\exp(-\tau_{ER}-\tau_{AR})\sigma\Phi(\theta)\,. \end{aligned} \tag{A.9}$$

At this point, we replace the scattering coefficient by the corresponding expression, whether we consider the Rayleigh scattering on air molecules, or the Mie scattering on aerosols. This gives

$$F_A^{ray} = \frac{L_E}{4\pi}\frac{A_E}{d_{ER}^2}\frac{\Sigma}{d_{AR}^2}\exp(-\tau_{ER}-\tau_{AR})\Gamma\beta\Phi_{ray}(\theta) \tag{A.10}$$

and

$$F_A^{aer} = \frac{L_E}{4\pi}\frac{A_E}{d_{ER}^2}\frac{\Sigma}{d_{AR}^2}\exp(-\tau_{ER}-\tau_{AR})\Gamma\bar{\omega}C_{ext}\Phi_{aer}(\theta)\,. \tag{A.11}$$

Table A.4
Parameters used in Eq. (A.15) (Bucholtz, 1995).

Coefficient	$0.2 < \lambda$ (μm) < 0.5	$0.5 < \lambda$ (μm)
A_{ray}	7.68246×10^{-4}	10.21675×10^{-4}
A_{op}	6.49997×10^{-3}	8.64145×10^{-3}
B	3.55212	3.99668
C	1.35579	0.00110298
D	0.11563	0.0271393

The total radiant flux measured by our virtual instrument is then the sum of both contributions as

$$F_A = \frac{L_E}{4\pi}\frac{A_E}{d_{ER}^2}\frac{\Sigma}{d_{AR}^2}\,\Gamma\,\exp(-\tau_{ER}-\tau_{AR})\left[\beta\Phi_{ray}(\theta) + \bar{\omega}C_{ext}\Phi_{aer}(\theta)\right]\,. \tag{A.12}$$

We describe below in more detail the computations of all the physical quantities used to compute F_A. Classically, the Rayleigh scattering cross section per molecule is (Rayleigh, 1871; Mie, 1908; Bucholtz, 1995)

$$C^{ray} = \frac{24\pi^3}{\lambda^4 N_s^2}\left(\frac{m_s^2-1}{m_s^2+2}\right)^2\frac{6+3\rho_n}{6-7\rho_n}\,, \tag{A.13}$$

with λ the wavelength, N_s the molecular number density for standard air, m_s the refractive index of standard air at λ and ρ_n the depolarization factor. In our model, this is accounted for via the Rayleigh scattering coefficient $\beta(\lambda, z)$ (in m^{-1}). Following Bucholtz (1995), it is approximated as

$$\beta(\lambda, z) = \beta_0(\lambda)\frac{P(z)}{P_0}\frac{T_0}{T(z)}\,, \tag{A.14}$$

with $P(z)$ and $T(z)$ the atmospheric pressure and temperature profiles. $P_0 = 101\,325$ Pa and $T_0 = 288.15$ K are the pressure and temperature at sea level, and

$$\beta_0(\lambda) = A_{ray}\lambda^{-(B+C\lambda+D/\lambda)}\,, \tag{A.15}$$

with λ the wavelength (in μm). This approximation takes into account the depolarization (or King) factor. Values for coefficients A_{ray}, B, C and D are given in Table A.4, and $\beta(\lambda, z)_{|z=0}$ is shown in Fig. A.13.

The effective optical depth τ of the atmosphere between E and R (and similarly between R and A), is the sum of three contributions from Rayleigh scattering, ozone absorption and aerosol extinction:

$$\tau = \tau_{ray} + \tau_{O_3} + \tau_{aer}\,. \tag{A.16}$$

The optical depth from Rayleigh scattering between E and R at respective altitudes z_E and z_R is (Bucholtz, 1995)

$$\tau_{ray}(z_E, z_R, \lambda) = \tau_0(\lambda)\frac{|P(z_E) - P(z_R)|}{P_0}\,, \tag{A.17}$$

where $\tau_0(\lambda)$ follows Eq. (A.15) with A_{ray} replaced by A_{op} (value given in Table A.4). The optical depth for ozone absorption is

$$\tau_{O_3}(z_E, z_R, \lambda) = \sigma_{O_3}(\lambda)\int_{z_E}^{z_R} N_{O_3}(z')dz'\,, \tag{A.18}$$

where $N_{O_3}(z)$ is the ozone number density at altitude z (provided with the atmospheric profile, see Fig. 2) and $\sigma_{O_3}(\lambda)$ (shown in Fig. A.13) is the ozone absorption cross section at wavelength λ and a fixed temperature of 273 K (Burrows et al., 1999). This is an approximation which could be refined in future versions with a dependence on temperature. The optical depth for aerosols is

$$\tau_{aer}(z_E, z_R, \lambda) = \int_{z_E}^{z_R} C_{ext}^{aer}(z', \lambda)dz'\,. \tag{A.19}$$

A.2. Computation of the polarization parameters of the light reaching the virtual instrument

To compute the $DoLP$ and $AoLP$ of the light reaching the virtual instrument, one must use the Stokes parameters I, Q and U. In the case

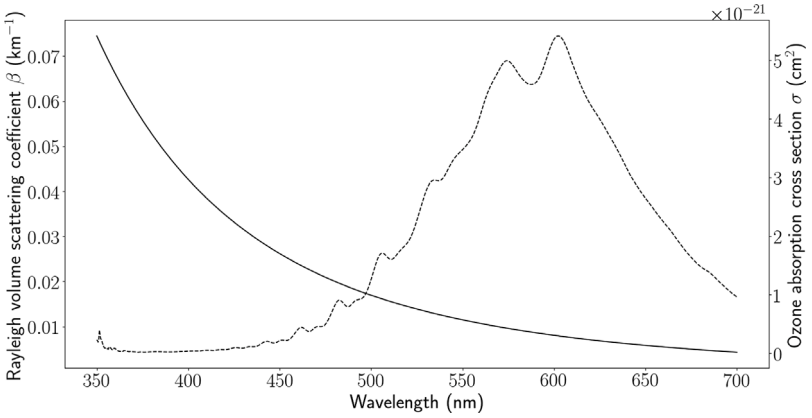

Fig. A.13. Rayleigh scattering coefficient at sea level $\beta_0(\lambda) = \beta(\lambda, z)_{|z=0}$ (full line, left, see Eq. (A.14)), and ozone absorption cross section $\sigma_{O_3}(\lambda)$ (dashed line, right), as a function of wavelength.

of light coming from a single point source and scattered at a single point along the line of sight, the polarization is defined with respect to the scattering plane containing the incoming and scattered rays. In this case, the polarization induced by Rayleigh and Mie scattering can only be either perpendicular or parallel to the scattering plane. So we assume $U = 0$. For example, the $DoLP$ of a light beam scattered at an angle θ via Rayleigh scattering is (McFarlane, 1974)

$$DoLP^{ray}(\theta) = |Q^{ray}(\theta)| = \frac{\sin^2\theta}{1+\cos^2\theta}\,. \tag{A.20}$$

and is always perpendicular to the scattering plane (which means that $AoLP = 0°$, $Q > 0$ and $U = 0$). We use the Lorentz–Mie scattering theory to compute the polarization induced by aerosol scattering. Here, we have the three Stokes parameters coding for linear polarization defined with respect to the scattering plane: I_s (computed in the previous section), Q_s computed from Rayleigh and Lorenz–Mie scattering theory and $U_s = 0$. These translate to a radiant flux (see previous section), a $DoLP_s = |Q_s|$ and an $AoLP_s = 0$ or 90° depending on the sign of Q_s. However, note that the orientation of the scattering plane is different for each point source in the input emission map. Therefore, it is not possible to add the Stokes parameters of each single contribution directly. Before, we must harmonize the definition of the polarization so that each single contribution is defined with respect to the same orientation. For this, we use a reference frame attached to the instrument defined as $\mathcal{R}_* = (\mathbf{x}_*, \mathbf{y}_*, \mathbf{z}_*)$ such that $\mathbf{x}_*$ points along the line of sight and $\mathbf{y}_*$ is horizontal in the plane of the detector. With this, we can express the normal vector of the instrument's plane of reference as $n = (0, 0, 1)$. This orientation is chosen so that, when the instrument points horizontally, $AoLP = 0°$ for a vertical polarization and $AoLP = 90°$ for a horizontal polarization. The scattering plane normal vector can be expressed as $(0, y_s, z_s)$ in this reference frame. All necessary derivations of y_s and z_s from the instrument pointing direction and the light source relative position are detailed by Bosse et al. (2020) in their appendix C. We define the $AoLP$ measured by the instrument as $0.5\arctan(y_s/z_s)$ in the case where $Q_s > 0$ (or $0.5\arctan(z_s/y_s)$ for $Q_s < 0$). The $AoLP$ is positive in the trigonometric direction (anti-clockwise) when looking towards the source. The $AoLP$ is π periodic, such that we define it in the interval $[-90°, 90°]$. The transformation of the Stokes parameters from one reference plane to the other corresponds to a rotation of the scattering plane to align to the instrument plane of reference. The 2D rotation matrix for an angle α is expressed as

$$R(\alpha) = \begin{pmatrix} \cos\alpha & \sin\alpha \\ -\sin\alpha & \cos\alpha \end{pmatrix}. \tag{A.21}$$

So the Stokes parameters in the reference plane of the instrument can be computed as:

$$\begin{pmatrix} Q \\ U \end{pmatrix} = R(2\,AoLP) \begin{pmatrix} Q_s \\ U_s \end{pmatrix}. \tag{A.22}$$

Only when the Stokes parameters for each single contribution have been rotated to match the global reference frame, one can sum the Stokes parameters to obtain the total polarization measured by the virtual instrument, such as described in Eq. (8). We finally can use (5) to convert the Stokes parameters to the $DoLP$ and $AoLP$ notation.

References

Amm, O., Viljanen, A., 1999. Ionospheric disturbance magnetic field continuation from the ground to the ionosphere using spherical elementary current systems. Earth Planets Space 51 (6), 431–440.

Ångström, A., 1929. On the atmospheric transmission of sun radiation and on dust in the air. Geografiska Annaler 11, 156–166. http://dx.doi.org/10.2307/519399.

Banks, P.M., Kockarts, G., 1973. Aeronomy. Springer.

Bellisario, C., Keckhut, P., Blanot, L., Hauchecorne, A., Simoneau, P., 2014. O2 and OH night airglow emissions derived from GOMOS-EnvisatInstrument. J. Atmos. Ocean. Technol. 31 (6), 1301–1311. http://dx.doi.org/10.1175/JTECH-D-13-00135.1.

Bellisario, C., Simoneau, P., Keckhut, P., Hauchecorne, A., 2020. Comparisons of spectrally resolved nightglow emission locally simulated with space and ground level observations. J. Space Weather Space Clim. 10, 21. http://dx.doi.org/10.1051/swsc/2020017.

Bergstrom, R.W., Pilewskie, P., Schmid, B., Russell, P.B., 2003. Estimates of the spectral aerosol single scattering Albedo and Aerosol radiative effects during SAFARI 2000. J. Geophys. Res.: Atmos. 108 (D13).

Berk, A., Hawes, F., 2017. Validation of MODTRAN®6 and its line-by-line algorithm. J. Quant. Spectrosc. Radiat. Transfer 203, 542–556. http://dx.doi.org/10.1016/j.jqsrt.2017.03.004.

Bommier, V., Sahal-Brechot, S., Dubau, J., Cornille, M., 2011. The theoretical impact polarisation of the O I 6300 å red line of earth aurorae. p. 9.

Born, M., Wolf, E., 1999. Principles of optics : electromagnetic theory of propagation, interference and diffraction of light.

Bosse, L., Lilensten, J., Gillet, N., Brogniez, C., Pujol, O., Rochat, S., Delboulbé, A., Curaba, S., Johnsen, M.G., 2022a. At the source of the polarisation of auroral emissions: Experiments and modeling. J. Space Weather Space Clim. 12, 7. http://dx.doi.org/10.1051/swsc/2022004.

Bosse, L., Lilensten, J., Gillet, N., Rochat, S., Delboulbé, A., Curaba, S., Roux, A., Magnard, Y., Johnsen, M.G., Løvhaug, U.-P., Amblard, P.-O., Bihan, N.L., Nabon, M., Marif, H., Auriol, F., Noûs, C., 2020. On the nightglow polarisation for space weather exploration. J. Space Weather Space Clim. 10, 35. http://dx.doi.org/10.1051/swsc/2020036.

Bosse, L., Lilensten, J., Johnsen, M.G., Gillet, N., Rochat, S., Delboulbé, A., Curaba, S., Ogawa, Y., Derverchère, P., Vauclair, S., 2022b. The polarisation of auroral emissions: A tracer of the E region ionospheric currents. J. Space Weather Space Clim. 12, 17. http://dx.doi.org/10.1051/swsc/2022014.

Bourgeois, S., Bosse, L., Lilensten, J., Gillet, N., Curaba, S., Delboulbé, A., Rochat, S., 2022. Laboratory experiments confirm the polarization of auroral emissions. Geophys. Res. Lett. http://dx.doi.org/10.1029/2022GL098707, e2022GL098707.

Broadfoot, A.L., Kendall, K.R., 1968. The Airglow spectrum, 3100-10,000 A. J. Geophys. Res. 73 (1), 426–428. http://dx.doi.org/10.1029/JA073i001p00426.

Bucholtz, A., 1995. Rayleigh-scattering calculations for the terrestrial atmosphere. Appl. Opt. 34 (15), 2765–2773. http://dx.doi.org/10.1364/AO.34.002765.

Burrows, J.P., Richter, A., Dehn, A., Deters, B., Himmelmann, S., Voigt, S., Orphal, J., 1999. Atmospheric remote-sensing reference data from gome– 2. temperature-dependent absorption cross sections of 3 in the 231–794nm range. J. Quant. Spectrosc. Radiat. Transfer 61 (4), 509–517. http://dx.doi.org/10.1016/S0022-4073(98)00037-5.

Chandrasekhar, S., 1960. Radiative Transfer. Dover Publications Inc., URL http://archive.org/details/RadiativeTransfer.

Dubovik, O., Smirnov, A., Holben, B.N., King, M.D., Kaufman, Y.J., Eck, T.F., Slutsker, I., 2000. Accuracy assessments of aerosol optical properties retrieved from aerosol robotic network (AERONET) sun and sky radiance measurements. J. Geophys. Res.: Atmos. 105 (D8), 9791–9806. http://dx.doi.org/10.1029/2000JD900040.

Dudhia, A., 2017. The reference forward model (RFM). J. Quant. Spectrosc. Radiat. Transfer 186, 243–253. http://dx.doi.org/10.1016/j.jqsrt.2016.06.018.

Dymond, K.F., Nicholas, A.C., Budzien, S.A., Stephan, A.W., Coker, C., Hei, M.A., Groves, K.M., 2019. A comparison of electron densities derived by tomographic inversion of the 135.6-nm ionospheric nightglow emission to incoherent scatter radar measurements. J. Geophys. Res. (Space Phys.) 124 (6), 4585–4596. http://dx.doi.org/10.1029/2018JA026412.

Elvidge, C., Baugh, K., Zhizhin, M., Hsu, F.-C., 2013. Why VIIRS data are superior to DMSP for mapping nighttime lights, Proc. Asia-Pacific Adv. Netw. 35, 62–69, http://dx.doi.org/10.7125/APAN.35.7.

Emde, C., Barlakas, V., Cornet, C., Evans, F., Korkin, S., Ota, Y., Labonnote, L.C., Lyapustin, A., Macke, A., Mayer, B., Wendisch, M., 2015. IPRT polarized radiative transfer model intercomparison project – phase a. J. Quant. Spectrosc. Radiat. Transfer 164, 8–36. http://dx.doi.org/10.1016/j.jqsrt.2015.05.007.

Falchi, F., Cinzano, P., Duriscoe, D., Kyba, C.C.M., Elvidge, C.D., Baugh, K., Portnov, B.A., Rybnikova, N.A., Furgoni, R., 2016. The new world atlas of artificial night sky brightness. Sci. Adv. 2 (6), e1600377. http://dx.doi.org/10.1126/sciadv.1600377.

Finlay, C.C., Olsen, N., Kotsiaros, S., Gillet, N., Tøffner-Clausen, L., 2016. Recent geomagnetic secular variation from swarm and ground observatories as estimated in the CHAOS-6 geomagnetic field model. Earth Planets Space 68 (1), http://dx.doi.org/10.1186/s40623-016-0486-1.

Garcia-Saenz, A., Sanchez de Miguel, A., Espinosa, A., Crespo, A., Aragonés, N., Llorca, J., Amiano, P., Martín, V., Guevara, M., Capelo, R., Tardón, A., Peiró, R., Jiménez-Moleón, J., Roca Barcelo, A., Perez-Gomez, B., Dierssen-Sotos, T., Fernández, T., Moreno-Iribas, C., Moreno, V., Kogevinas, M., 2018. Evaluating the association between artificial light-at-night exposure and breast and prostate cancer risk in Spain (MCC-Spain study). Environ. Health Perspect. 126, http://dx.doi.org/10.1289/EHP1837.

Grubisic, M., van Grunsven, R., Kyba, C., Manfrin, A., Hölker, F., 2018. Insect declines and agroecosystems: Does light pollution matter? Ann. Appl. Biol. 173, 180–189. http://dx.doi.org/10.1111/aab.12440.

Hänel, A., Posch, T., Ribas, S.J., Aubé, M., Duriscoe, D., Jechow, A., Kollath, Z., Lolkema, D.E., Moore, C., Schmidt, N., Spoelstra, H., Wuchterl, G., Kyba, C.C.M., 2018. Measuring night sky brightness: Methods and challenges. J. Quant. Spectrosc. Radiat. Transfer 205, 278–290. http://dx.doi.org/10.1016/j.jqsrt.2017.09.008.

Hansen, J.E., 1971. Multiple scattering of polarized light in planetary atmospheres part II. Sunlight reflected by terrestrial water clouds. J. Atmos. Sci. 28 (8), 1400–1426.

Hasekamp, O.P., 2010. Capability of multi-viewing-angle photo-polarimetric measurements for the simultaneous retrieval of Aerosol and cloud properties. Atmos. Meas. Tech. 3 (4), 839–851. http://dx.doi.org/10.5194/amt-3-839-2010.

Horvath, G., Kriska, G., Malik, P., Robertson, B., 2009. Polarized light pollution: A new kind of ecological photopollution. Front. Ecol. Environ. 7, 317–325. http://dx.doi.org/10.1890/080129.

Hovenier, J.W., 1971. Multiple scattering of polarized light in planetary atmospheres. Astron. Astrophys. 13, 7.

Hovenier, J.W., 1971. Multiple scattering of polarized light in planetary atmospheres. Astron. Astrophys. 13, 7.

Jaenicke, R., 1993. Chapter 1 tropospheric aerosols. In: International Geophysics, Vol. 54. Elsevier, pp. 1–31. http://dx.doi.org/10.1016/S0074-6142(08)60210-7.

Kriska, G., Horváth, G., Andrikovics, S., 1998. Why do mayflies lay their eggs en masse on dry Asphalt roads? water-imitating polarized light reflected from Asphalt attracts ephemeroptera.. J. Exp. Biol. 201 (15), 2273–2286. http://dx.doi.org/10.1242/jeb.201.15.2273.

Kyba, C., Kuester, T., Sanchez de Miguel, A., Baugh, K., Jechow, A., Hölker, F., Bennie, J., Elvidge, C., Gaston, K., Guanter, L., 2017. Artificially lit surface of earth at night increasing in radiance and extent. Sci. Adv. 3, e1701528. http://dx.doi.org/10.1126/sciadv.1701528.

Kyba, C., Ruhtz, T., Fischer, J., Hölker, F., 2011. Lunar skylight polarization signal polluted by urban lighting. J. Geophys. Res. (Atmos.) 116, 24106. http://dx.doi.org/10.1029/2011JD016698.

Leinert, C., Bowyer, S., Haikala, L.K., Hanner, M.S., Hauser, M.G., Levasseur-Regourd, A.-C., Mann, I., Mattila, K., Reach, W.T., Schlosser, W., Staude, H.J., Toller, G.N., Weiland, J.L., Weinberg, J.L., Witt, A.N., 1998. The 1997 reference of diffuse night sky brightness. Astron. Astrophys. Suppl. Ser. 127 (1), 1–99. http://dx.doi.org/10.1051/aas:1998105.

Lilensten, J., Barthélemy, M., Besson, G., Lamy, H., Johnsen, M.G., Moen, J., 2016. The thermospheric auroral red line angle of linear polarization: auroral angle of linear polarization. J. Geophys. Res. Space Phys. 121 (7), 7125–7134. http://dx.doi.org/10.1002/2016JA022941.

Lilensten, J., Moen, J., Barthélemy, M., Thissen, R., Simon, C., Lorentzen, D.A., Dutuit, O., Amblard, P.O., Sigernes, F., 2008. Polarization in Aurorae: A new dimension for space environments studies. Geophys. Res. Lett. 35 (8), http://dx.doi.org/10.1029/2007GL033006.

Lorenz, L., 1890. Lysbevaegelsen i og uden for en af plane Lysbolger belyst Kugle". Det Kongelige Danske Videnskabernes Selskabs Skrifter. 66. Bind 1. pp. 1–62.

McFarlane, S.C., 1974. A bethe theory for the polarization of impact radiation. J. Phys. B Atom. Mol. Phys. 7 (13), 1756–1771. http://dx.doi.org/10.1088/0022-3700/7/13/021.

Mie, G., 1908. Beiträge Zur Optik Trüber Medien, Speziell Kolloidaler Metallösungen. Ann. Der Phys. 330 (3), 377–445. http://dx.doi.org/10.1002/andp.19083300302.

Miller, S.D., Straka, W., Mills, S.P., Elvidge, C.D., Lee, T.F., Solbrig, J., Walther, A., Heidinger, A.K., Weiss, S.C., 2013. Illuminating the capabilities of the Suomi national polar-orbiting partnership (NPP) visible infrared imaging radiometer suite (VIIRS) day/Night Band. Remote Sens. 5 (12), 6717–6766. http://dx.doi.org/10.3390/rs5126717.

Mills, S., Weiss, S., Liang, C., 2013. VIIRS day/night band (DNB) stray light characterization and correction. In: Butler, J.J., Xiong, X.J., Gu, X. (Eds.), SPIE Optical Engineering + Applications. San Diego, California, United States, p. 88661P. http://dx.doi.org/10.1117/12.2023107.

Mishchenko, M.I., Travis, L.D., Lacis, A.A., 2002. Scattering, Absorption, and Emission of Light By Small Particles. Cambridge University Press.

Parihar, N., Radicella, S.M., Nava, B., Migoya-Orue, Y.O., Tiwari, P., Singh, R., 2018. An investigation of the ionospheric F region near the EIA crest in India using OI 777.4 and 630.0 nm nightglow observations. Ann. Geophys. 36 (3), 809–823. http://dx.doi.org/10.5194/angeo-36-809-2018.

Petržala, J., 2021. Revision of path-integral approach to radiative transfer. J. Quant. Spectrosc. Radiat. Transfer 107670. http://dx.doi.org/10.1016/j.jqsrt.2021.107670.

Plane, J., Oetjen, H., de Miranda, M., Saiz-Lopez, A., Gausa, M., Williams, B., 2012. On the sodium D line emission in the terrestrial nightglow. J. Atmos. Sol.-Terr. Phys. 74, 181–188. http://dx.doi.org/10.1016/j.jastp.2011.10.019.

Pulkkinen, A., Amm, O., Viljanen, A., 2003. Ionospheric equivalent current distributions determined with the method of spherical elementary current systems. J. Geophys. Res. Space Phys. 108 (A2).

Pust, N.J., Shaw, J.A., 2011. Comparison of skylight polarization measurements and MODTRAN-P calculations. J. Appl. Rem. Sens. 5, 18.

Ramella-Roman, J.C., Prahl, S.A., Jacques, S.L., 2005. Three Monte Carlo programs of polarized light transport into scattering media: part I. Opt. Express 13 (12), 4420–4438.

Rayleigh, J.W.S.B., 1871. On the scattering of light by small particles. Lond. Edinb. Dublin Philos. Mag. J. Sci. 41, 447—454. http://dx.doi.org/10.1080/14786447108640507.

Remedios, J., Leigh, R., Waterfall, A., Moore, D., Sembhi, H., Parkes, I., Greenhough, J., Chipperfield, M., Hauglustaine, D., 2007. MIPAS reference atmospheres and comparisons to V4. 61/V4. 62 MIPAS level 2 geophysical data sets [dataset]. Atmos. Chem. Phys. Discuss. 7 (4), 9973–10017.

Snik, F., Rietjens, J.H.H., Apituley, A., Volten, H., Mijling, B., Di Noia, A., Heikamp, S., Heinsbroek, R.C., Hasekamp, O.P., Smit, J.M., Vonk, J., Stam, D.M., van Harten, G., de Boer, J., Keller, C.U., iSPEX citizen Scientists, 3187, 2014. Mapping atmospheric aerosols with a citizen science network of smartphone spectropolarimeters. Geophys. Res. Lett. 41 (20), 7351–7358. http://dx.doi.org/10.1002/2014GL061462.

Staude, H., 1975. Scattering in the earth's atmosphere: Calculations for milky way and zodiacal light as extended sources. Astron. Astrophys. 39, 325.

Tadono, T., Nagai, H., Ishida, H., Oda, F., Naito, S., Minakawa, K., Iwamoto, H., 2016. Generation of the 30 m-mesh global digital surface model by alos prism, XLI-B4, 157–162, http://dx.doi.org/10.5194/isprs-archives-XLI-B4-157-2016. https://doaj.org, The International Archives of the Photogrammetry, Remote Sensing and Spatial Information Sciences.

Tashchilin, A., Leonovich, L., 2016. Modeling nightglow in atomic oxygen red and green lines under moderate disturbed geomagnetic conditions at midlatitudes. Solar-Terrestrial Phys. 2 (4), 94–106. http://dx.doi.org/10.12737/21491.

Tomasko, M.G., Doose, L.R., Dafoe, L.E., See, C., 2009. Limits on the size of aerosols from measurements of linear polarization in Titan's atmosphere. Icarus 204 (1), 271–283. http://dx.doi.org/10.1016/j.icarus.2009.05.034.

Ugolnikov, O.S., Postylyakov, O.V., Maslov, I.A., 2004. Effects of multiple scattering and atmospheric aerosol on the polarization of the twilight sky. J. Quant. Spectrosc. Radiat. Transfer 88, 233–241. http://dx.doi.org/10.1016/j.jqsrt.2003.12.033.

van de Hulst, H.C., 1981. Light Scattering By Small Particles. Dover Publications, New York.

Vargas, F., 2019. Traveling ionosphere disturbance signatures on ground-based observations of the O(^{1}D) nightglow inferred from 1-D modeling. J. Geophys. Res. (Space Phys.) 124 (11), 9348–9363. http://dx.doi.org/10.1029/2019JA027356.

Wang, J., Aegerter, C., Xu, X., Szykman, J.J., 2016. Potential application of VIIRS day/Night Band for monitoring nighttime surface PM2.5 air quality from space. Atmos. Environ. 124, 55–63. http://dx.doi.org/10.1016/j.atmosenv.2015.11.013.

Wang, J., Zhou, M., Xu, X., Roudini, S., Sander, S.P., Pongetti, T.J., Miller, S.D., Reid, J.S., Hyer, E., Spurr, R., 2020. Development of a nighttime shortwave radiative transfer model for remote sensing of nocturnal aerosols and fires from VIIRS. Remote Sens. Environ. 241, 111727. http://dx.doi.org/10.1016/j.rse.2020.111727.

Yong, H., Guo-Dong, S., Ke-Yong, Z., 2016. Backward and forward Monte Carlo method in polarized radiative transfer. Astrophys. J. 820 (1), 9. http://dx.doi.org/10.3847/0004-637X/820/1/9.

Zhou, M., Wang, J., Chen, X., Xu, X., Colarco, P.R., Miller, S.D., Reid, J.S., Kondragunta, S., Giles, D.M., Holben, B., 2021. Nighttime smoke aerosol optical depth over U.S. Rural areas: First retrieval from VIIRS moonlight observations. Remote Sens. Environ. 267, 112717. http://dx.doi.org/10.1016/j.rse.2021.112717.

Zielinska-Dabkowska, K., 2018. Make lighting healthier. Nature 553, http://dx.doi.org/10.1038/d41586-018-00568-7.